

Anisotropic strong lensing as a probe of dark matter self-interactions

Birendra Dhanasingham¹★, Francis-Yan Cyr-Racine¹†, Charlie Mace^{2,3,4}, Annika H. G. Peter^{2,3,4,5}, and Andrew Benson⁶

¹*Department of Physics and Astronomy, University of New Mexico, 210 Yale Blvd NE, Albuquerque, NM 87106, USA*

²*Department of Physics, The Ohio State University, 191 W. Woodruff Ave., Columbus, OH 43210, USA*

³*Center for Cosmology and Astroparticle Physics, The Ohio State University, 191 W. Woodruff Ave., Columbus, OH 43210, USA*

⁴*Department of Astronomy, The Ohio State University, 140 W. 18th Ave., Columbus, OH 43210, USA*

⁵*School of Natural Sciences, Institute for Advanced Study, 1 Einstein Drive, Princeton, NJ 08540, USA*

⁶*Carnegie Observatories, 813 Santa Barbara Street, Pasadena, CA 91101, USA*

Accepted 2023 October 6. Received 2023 September 27; in original form 2023 June 26

ABSTRACT

Galaxy-scale strongly lensed systems have been shown to provide a unique technique for exploring the underlying physics of dark matter at sub-galactic scales. In the past, much attention was given to detecting and studying individual haloes in a strong lens system. In addition to the subhaloes, line-of-sight haloes contribute significantly to the small perturbations in lensed images. In prior work, we demonstrated that these line-of-sight haloes imprint a distinctive anisotropic signature and hence give rise to a detectable non-zero parity-even quadrupole moment in the effective convergence field’s two-point correlation function. In this study, we show that these line-of-sight haloes also produce a non-zero curl component of the effective deflection field with a parity-odd quadrupole moment of the two-point function. These multipole moments have the ability to statistically separate line-of-sight haloes from dark matter substructure. In this paper, we examine how these multipole moments evolve in the presence of warm dark matter and self-interacting dark matter in terms of central density evolution and dark matter halo abundance. Importantly, we show that these different multipole moments display exquisite sensitivity to both the amplitude and the velocity dependence of the dark matter self-interaction cross-section. Our approach opens the door for strong lensing observations to probe dark matter self-interaction over a broad range of relative velocities.

Key words: gravitational lensing: strong – methods: numerical – galaxies: haloes – dark matter

1 INTRODUCTION

Alternative models to the Lambda cold dark matter (Λ CDM) model have gained popularity as potential tools for understanding the Λ CDM model’s inadequacies in the non-linear regime (see e.g., Bullock & Boylan-Kolchin 2017). For instance, self-interacting dark matter (SIDM) (Spergel & Steinhardt 2000; Tulin et al. 2013b,a; Rocha et al. 2013; Peter et al. 2013; Kaplinghat et al. 2013, 2014a,b, 2016; Elbert et al. 2015; Burger & Zavala 2019), in which dark matter particles can transfer momentum and energy through scattering, is characterized by haloes with a different density profile as compared to CDM. This profile could be either cored if the interaction cross-section is not too large and haloes are not too evolved, or very dense and steep if the haloes enter the gravothermal-collapse regime (Lynden-Bell & Wood 1968; Balberg et al. 2002; Balberg & Shapiro 2002; Ahn & Shapiro 2005; Kahlhoefer et al. 2019; Nishikawa et al. 2020; Gilman et al. 2021; Zeng et al. 2022; Meshveliani et al. 2023; Yang & Yu 2022; Yang et al. 2023a,b; Zhong et al. 2023).

Another possibility is that warm dark matter (WDM), which deviates from the hierarchical structure formation of the Λ CDM picture,

exhibits a tiny abundance of low-mass dark matter haloes because free streaming effects erase the small density perturbations below a characteristic length scale (Bond & Szalay 1983; Bode et al. 2001; Dalcanton & Hogan 2001; Schneider et al. 2013; Viel et al. 2013; Benson et al. 2013; Pullen et al. 2014; Lovell 2020). The suppression of the abundance of WDM haloes and the core or cuspy central densities of SIDM haloes considerably impact the subtle perturbations in a strong lensed image, making galaxy-scale strong lens systems a powerful tool for studying different dark matter models.

Strong gravitational lensing is a promising method for probing the distribution of dark matter on sub-galactic scales and at redshifts higher than the Local Group of galaxies (see e.g., Mao & Schneider 1998; Chiba 2002; Dalal & Kochanek 2002; Metcalf & Zhao 2002; Kochanek & Dalal 2003; Keeton 2003; Kochanek & Dalal 2004; Koopmans 2005). A close analysis of these strongly lensed images (see e.g., Bolton et al. 2006, 2008; Gavazzi et al. 2008; Auger et al. 2009; Brownstein et al. 2012; Shu et al. 2016; Oldham et al. 2017; Cornachione et al. 2018; Lemon et al. 2020) reveals small localized gravitational perturbations beyond the smooth mass distribution of the main lens galaxy, which are mostly caused by the main lens substructure or line-of-sight haloes distributed between the observer and the source. A careful examination of these subtle perturbations has the potential to disclose the physics underneath these small-scale

★ E-mail: birendradh@unm.edu

† E-mail: fycr@unm.edu

structures (Vegetti & Koopmans 2009a,b; Xu et al. 2012; Vegetti et al. 2010a,b, 2012; Vegetti & Vogelsberger 2014; Li et al. 2017; Hezaveh et al. 2016a; Minor et al. 2017; Gilman et al. 2019, 2020a,b; Amorisco et al. 2022; Minor et al. 2021a,b; Şengül et al. 2022; Şengül & Dvorkin 2022; Laroche et al. 2022; Hogg et al. 2023; Keeley et al. 2023; Vegetti et al. 2023).

When considering the collective effect of multiple lens planes in a strong lens system, Dhanasingham et al. (2023) pointed out that the dark matter substructure and line-of-sight haloes contribute differently to the two lensing potentials discussed under the effective multiplane gravitational lensing formalism. In this approach, the effective deflection field is decomposed into a gradient of an effective scalar potential and the curl of an effective vector potential, where the latter is zero under single-plane lensing. Many previous studies on the weak lensing by large-scale structure on cosmic microwave background (CMB) temperature and polarization fluctuations took a similar approach, pointing out a rotation of these fluctuation fields by going beyond the Born approximation and into the post-Born regime (Cooray & Hu 2002; Hirata & Seljak 2003; Cooray et al. 2005; Robertson & Lewis 2023). In addition, Pen & Mao (2006) discussed the induced rotation of quadruply lensed sources in the presence of uncorrelated large-scale structure. In a strong lens system, the projected mass density derived by considering the curl of the effective deflection field is thus purely originating from line-of-sight objects, causing rotational distortion in the strongly lensed images.

According to Dhanasingham et al. (2023), unlike dark matter subhaloes, line-of-sight haloes leave distinctive anisotropic traces and quadrupole patterns in the two-dimensional projected mass density field. In this work, we measure the distinct quadrupole signature on the two-point function imprinted by these haloes in the presence of WDM and SIDM. Many earlier papers have proposed the use of angular-averaged two-point function monopole as a feasible tool for studying dark matter physics on sub-galactic scales (see e.g., Hezaveh et al. 2016b; Chatterjee & Koopmans 2018; Díaz Rivero et al. 2018a,b; Brennan et al. 2019; Cyr-Racine et al. 2019; Çağan Şengül et al. 2020; Bayer et al. 2023a,b). In addition to this monopole generated by both substructure and line-of-sight haloes, we focus for the first time on anisotropic imprints generated by isolated line-of-sight haloes with two different dark matter theories. This effort will be useful in testing and improving our understanding of dark matter microphysics in conjunction with many ground- and space-based surveys this decade to observe galaxy–galaxy strong lenses (Serjeant 2014; Collett 2015; Serjeant 2017; Metcalf et al. 2019; Weiner et al. 2020; Mao et al. 2022) and the development of machine learning algorithms to identify these strong lens systems (see e.g., Hezaveh et al. 2017; Perreault-Levasseur et al. 2017; Schaefer et al. 2018; Vernardos et al. 2020; Cheng et al. 2020; Li et al. 2020; Ostdiek et al. 2022a,b; Legin et al. 2022; Wilde et al. 2022; Rezaei et al. 2022; Zhang et al. 2022; Adam et al. 2023; Wagner-Carena et al. 2023; Rojas et al. 2023; Canameras et al. 2023). In particular, as we will show in this paper, these various multipole moments are sensitive to both the amplitude and velocity dependence of the dark matter self-interaction cross-section. Since the purpose of this work is to demonstrate how different dark matter scenarios change the amplitude and shape of two-point correlation function multipoles rather than analyse specific known lensed systems, we focus below on relatively simple lens configurations. However, we emphasize that important aspects of observed strong lens systems (e.g., macrolens model, baryon disruption effects, etc.) will need to be carefully modelled in any realistic analyses, as they can impact the shape and amplitude of the two-point correlation function. We leave such a detailed analysis to future work.

In this work, `PYHALO`¹ (Gilman et al. 2021) is used to render dark matter substructure and line-of-sight haloes on top of the open-source PYTHON software package `LENSTRONOMY`² (Birrer & Amara 2018; Birrer et al. 2021) as the lensing computation tool. Based on the Planck 2018 (Planck Collaboration et al. 2020) results, we assume a flat Λ CDM cosmology throughout this work. Additionally, we set the redshift of the source to $z_s = 1.0$ and that of the primary lens to $z_{\text{macro}} = 0.5$. We take into account a power-law ellipsoid main lens mass profile with the Einstein radius $\theta_E = 1.0$ arcsec, the eccentricity components $(e_1, e_2) = (0.05, 0.08)$, and the logarithmic slope $\gamma = 2.078$ (Auger et al. 2010). The components of the external gravitational shear field caused by matter in the neighbourhood of this main lens are set to $(\gamma_1, \gamma_2) = (0.01, -0.01)$. We utilize the mass definition of M_{200} with regard to the critical density of the Universe at the halo redshift throughout this work.

This manuscript is organized as follows: In Section 2, we discuss how to generate dark matter halo realizations using the CDM, WDM, and SIDM frameworks, while accounting for free-streaming effects and dark matter self-interactions. Section 3 introduces the fundamental ideas of effective multiplane lensing and various angular and symmetry structures in effective deflection fields, as well as methods for quantifying anisotropies and symmetries. In Section 4, we discuss the impact of WDM and SIDM on strong lensing anisotropy measurements. Finally, in Section 5, we summarize our main findings and analyse the broad implications.

2 GENERATING DARK MATTER HALO REALIZATIONS

This section describes how to generate dark matter substructure and line-of-sight halo realizations considering the CDM, SIDM, and WDM frameworks.

2.1 Cold and warm dark matter haloes

Here we discuss our dark matter substructure and line-of-sight density profile choices, taking into account both the CDM and WDM scenarios, as well as the suppression of WDM halo central densities due to the free-streaming effect of WDM particles.

2.1.1 Halo density profiles

The CDM subhaloes are modelled as truncated Navarro–Frenk–White (TNFW) profiles (Baltz et al. 2009) in our study, and the substructure is tidally truncated using a Roche limit approximation. Moreover, we use NFW (Navarro et al. 1996) density profiles to simulate line-of-sight dark matter haloes and we compute the scale radii and densities using the mass–concentration relationship presented in Diemer & Joyce (2019) with a scatter in the concentration of 0.13 dex.

Unlike CDM haloes, WDM haloes are subject to free-streaming effects, as discussed in the following section. This effect alters the central densities of TNFW subhaloes and the NFW line-of-sight halo mass profiles of WDM haloes, and therefore we employ a rescaled version of the CDM mass–concentration relationship for WDM haloes to account for this free-streaming effects, as discussed further below.

¹ <https://github.com/dangilman/pyHalo>

² <https://github.com/lenstronomy>

2.1.2 Free-streaming and mass–concentration relation

The characteristic non-negligible thermal velocities of WDM particles in the early Universe result in the free streaming of particles that erase small density perturbations in the matter distribution below the free-streaming length and inhibiting the formation of the structure below this length-scale, thus suppressing the linear matter power spectrum on small scales. The free-streaming length directly depends on the thermal velocity distribution of the dark matter particles and hence the WDM particle mass and formation mechanism (Bond & Szalay 1983; Schneider et al. 2013; Benson et al. 2013).

The half-mode mass, m_{hm} , which is defined in terms of the power spectrum wave number where the WDM transfer function relative to CDM is damped by 0.5, is frequently used to model the free-streaming effects on the WDM matter power spectrum. The abundance of WDM haloes is strongly suppressed below the half-mode mass as a result of free streaming, and WDM haloes also have a different internal structure than CDM haloes due to this effect. We discuss the free-streaming effects on the halo mass function in Section 2. In this work, we assume thermal relic WDM with particle mass m_{WDM} and thus use the relation between the half-mode mass and the dark matter mass $m_{\text{hm}} \propto m_{\text{WDM}}^{-3.33}$ (Schneider et al. 2012). When this relationship is normalized using the scaling $2 \times 10^8 M_{\odot} h^{-1} \sim 3.3 \text{keV}$ constrained from the Lyman- α flux power spectrum measurements presented in Viel et al. (2013), the half-mode mass may be written down as

$$m_{\text{hm}}(m_{\text{WDM}}) = 10^{10} \left(\frac{m_{\text{WDM}}}{1 \text{keV}} \right)^{-3.33} M_{\odot} h^{-1}. \quad (1)$$

In contrast to CDM haloes, the free-streaming effect limits the fine-grained phase space density of WDM haloes (Macciò et al. 2012; Shao et al. 2013), hence restricting the central density of these objects. Moreover, haloes below the half-mode mass form later in WDM models, when the Universe is less dense, and so have lower concentrations than in the CDM model. Because the subtle perturbations of lensed images caused by dark matter substructure and line-of-sight haloes are highly sensitive to dark matter halo central densities, suppression of halo concentration has an important effect on strong lensing observables. In this study, we implement the parametrization proposed by Bose et al. (2016) to model the free-streaming effects on the mass–concentration relationship of WDM haloes, which has the form

$$\frac{c_{\text{WDM}}(m, z)}{c_{\text{CDM}}(m, z)} = (1+z)^{\beta(z)} \left(1 + 60 \frac{m_{\text{hm}}}{m} \right)^{-0.17}, \quad (2)$$

where $\beta(z) = 0.026z - 0.04$. Here $c_{\text{CDM}}(m, z)$ is the CDM mass–concentration model from Diemer & Joyce (2019) with a scatter of 0.13 dex. Fig. 1 illustrates the mass–concentration relation for CDM and WDM models as a function of half-mode mass and the halo redshift. We observe that haloes with masses up to two orders of magnitude above m_{hm} have suppressed concentration in the WDM case. We incorporate this halo concentration suppression into our WDM models in order to derive more accurate dark matter predictions for strong lensing observables.

2.2 Self-interacting dark matter haloes

To generate the SIDM halo realizations, we utilize the model presented by Gilman et al. (2021). In this section, we present a brief overview of this SIDM model.

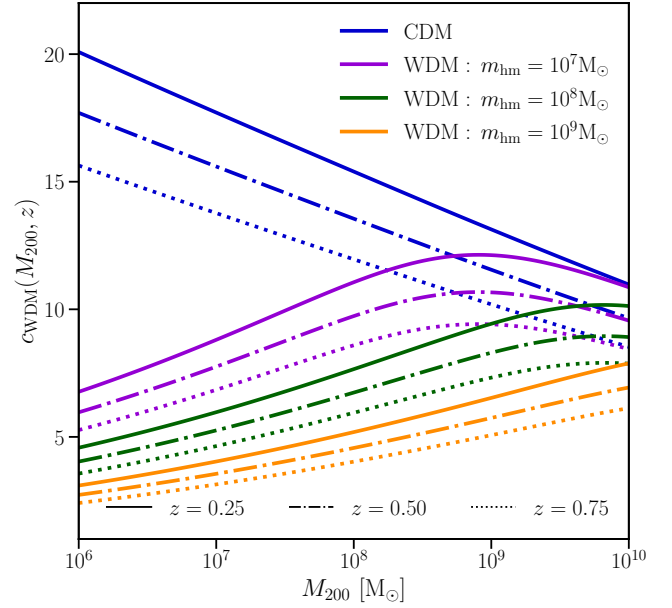


Figure 1. The mass–concentration relation for CDM and WDM models as a function of half-mode mass (m_{hm}) and the halo redshift (z).

2.2.1 Interaction cross-section

Let us first consider the simple velocity-dependent cross-section introduced by Gilman et al. (2021), which is parameterized as

$$\sigma(v) = \frac{\sigma_0}{\left(1 + \frac{v^2}{v_0^2} \right)^2}, \quad (3)$$

where v is the relative velocity of the dark matter particles, σ_0 is the normalization that determines the amplitude of the cross-section, and the $\sigma(v)$ behaves as $\sigma_v \propto v^{-4}$ beyond the characteristic velocity v_0 . This choice of interaction cross-section enables sizable scattering of dark matter particles at low relative velocities while avoiding the constraints on the cross-section at high velocities from galaxies and galaxy clusters (Peter et al. 2013; Kim et al. 2017; Robertson et al. 2019; Banerjee et al. 2020; Sagunski et al. 2021; McDaniel et al. 2021; Andrade et al. 2022; Eckert et al. 2022; Cross et al. 2023).

2.2.2 Core formation, core-collapse, and core-collapse probability

The presence of self-interactions can dramatically affect the internal dynamics of haloes by allowing different dark matter particles to exchange energy and momentum. In a standard NFW profile, the temperature and line-of-sight velocity dispersion of dark matter particles is greater towards the halo’s outskirts. The presence of self-interaction allows heat to flow in and dark matter particles to flow out until an isothermal density core is formed and the central velocity dispersion is equalized (Ahn & Shapiro 2005; Vogelsberger et al. 2012; Rocha et al. 2013; Elbert et al. 2015; Burger & Zavala 2019). This core has a high temperature relative to the halo outskirts, creating a gradient that now favours an outward heat flow. The core then begins to shrink while its density increases, due to the negative heat capacity of such a self-gravitating system. This rapid core collapse, also known as the gravothermal catastrophe, generates a sharp density cusp (Lynden-Bell & Wood 1968; Balberg et al. 2002; Balberg & Shapiro 2002).

According to [Nishikawa et al. \(2020\)](#), dark matter haloes subjected to tidal stripping exhibit accelerated core-collapse compared to isolated dark matter haloes. This faster core-collapse occurs after only $\mathcal{O}(10)t_0$, as opposed to the longer time-scales of $\mathcal{O}(100)t_0$ taken by isolated haloes, which did not experience any tidal forces during their evolution ([Kahlhoefer et al. 2019](#); [Nishikawa et al. 2020](#); [Sameie et al. 2020](#); [Correa 2021](#); [Zeng et al. 2022](#); [Yang & Yu 2022](#); [Yang et al. 2023b](#)). The time-scale for structure evolution t_0 here is determined by the values of σ_0 , scale density, and v_0 . The substructure and line-of-sight halo time scales are therefore set to $t_{\text{sub}} = 10t_0$ and $t_{\text{LOS}} = 100t_0$, respectively. Given the time since the halo's collapse t_{halo} , we adopt the probability of core-collapse introduced by [Gilman et al. \(2021\)](#), parameterized as:

$$P_{\text{collapse}} = \begin{cases} 0 & t_{\text{halo}} \leq 0.5t', \\ \frac{t_{\text{halo}} - t'}{t'} & t_{\text{halo}} \leq 2t', \\ 1 & t_{\text{halo}} > 2t', \end{cases} \quad (4)$$

where t' is either t_{LOS} or t_{sub} . It should be noted that this model is still approximate and has not yet been calibrated by simulations.

2.2.3 Density profiles of cored and core-collapsed haloes

We model the main galaxy substructure and line-of-sight dark matter haloes before the core-collapse as cored truncated NFW (cored-TNFW) profiles as

$$\rho(x, \beta, \tau) = \frac{\rho_s}{(x^a + \beta^a)^{\frac{1}{a}} (1+x)^2} \frac{\tau^2}{\tau^2 + x^2}, \quad (5)$$

where $x = r/r_s$, $\tau = r_t/r_s$, $\beta = r_c/r_s$, r_t is the truncation radius, r_c is the core radius, and r_s is the scale radius. Appendix A summarizes the procedure for computing the parameter β discussed in [Gilman et al. \(2021\)](#). We set the value of a to 10 and calculate the scale radius r_s and scale density ρ_s for an NFW profile using the mass-concentration relationship proposed by [Diemer & Joyce \(2019\)](#) with a scatter of 0.13 dex.

In order to model the steep central density cusps in core-collapsed dark matter haloes, we use the power-law density profile given by

$$\rho(r, r_c, x_{\text{match}}) = \rho_c(x_{\text{match}}) \left(1 + \frac{r^2}{r_c^2} \right)^{-\frac{\gamma}{2}}, \quad (6)$$

where γ is the logarithmic profile slope, ρ_c is the core density, and r_c is the core radius. The parameter x_{match} determines the density profile normalization ρ_c so that the enclosed mass of the NFW profile inside $x_{\text{match}}r_s$ matches the mass of the core-collapsed halo inside $x_{\text{match}}r_s$. In our model, the core radius r_c that keeps the total mass within r_s finite, is set to $0.05r_s$ and x_{match} and γ are set to 2.16 and 3.0, respectively.

2.3 Subhalo and line-of-sight halo mass functions

2.3.1 Populating CDM and SIDM haloes

Considering both the SIDM and the benchmark CDM models, we generate multiple random realizations of dark matter substructure and line-of-sight dark matter haloes with the masses of the haloes range from $10^6 M_\odot$ to $10^{10} M_\odot$, and $M_{\text{halo}} = 10^{13.3} M_\odot$ being the main halo mass. Here we omit haloes with masses greater than $10^{10} M_\odot$ from our realizations since these massive haloes are likely to have a baryonic mass component and so be observable or lead to a large

enough lensing effect to be directly included in the main lens model (see e.g., [Birrer et al. 2019](#)).

The subhaloes are populated using the power-law mass function given in equation (7) with a logarithmic slope of $\alpha = -1.90$ and a pivot mass of $m_0 = 10^8 M_\odot$. This value is compatible with previously predicted power-law slope values by N -body simulations ([Benson 2020](#); [Springel et al. 2008](#)). Given the halo mass m at infall and normalization $\Sigma_{\text{sub}} = 0.025 \text{ kpc}^{-2}$ ([Gilman et al. 2019, 2020a](#); [Nadler et al. 2021](#)), the subhalo mass function takes the form

$$\frac{d^2 N_{\text{sub,CDM}}}{dm dA} = \frac{d^2 N_{\text{sub,SIDM}}}{dm dA} = \frac{\Sigma_{\text{sub}}}{m_0} \left(\frac{m}{m_0} \right)^\alpha \mathcal{F}(M_{\text{halo}}, z). \quad (7)$$

Here

$$\log_{10}(\mathcal{F}) = k_1 \log_{10} \left(\frac{M_{\text{halo}}}{10^{13} M_\odot} \right) + k_2 \log_{10}(z + 0.5) \quad (8)$$

is the scaling function that determines the differential projected number density of the substructure as a function of host halo mass M_{halo} and redshift z , with $(k_1, k_2) = (0.88, 1.70)$ ([Gilman et al. 2020b](#)) predicted using the GALACTICUS semi-analytical model ([Benson 2012](#); [Pullen et al. 2014](#); [Yang et al. 2020](#)).

We render line-of-sight dark matter haloes in the previously specified mass range using the Sheth–Tormen (ST) mass function ([Sheth et al. 2001](#)) with two modifications proposed by [Gilman et al. \(2019\)](#). The first re-scaling factor δ_{LOS} proposed by [Gilman et al. \(2019\)](#) accounts for systematic fluctuations in the mean number of haloes predicted by the Sheth–Tormen mass function as well as baryonic effects on small-scale structure formation ([Gilman et al. 2020b](#); [Benson 2020](#)). The second factor $\xi_{2\text{halo}}$ is the two-halo term, which represents the influence of correlated structures in the vicinity of the host dark matter halo on the three-dimensional two-point correlation function ([Gilman et al. 2019](#); [Gilman et al. 2021](#); [Lazar et al. 2021](#)). Then the CDM and SIDM line-of-sight halo mass functions have the form

$$\begin{aligned} \frac{d^2 N_{\text{LOS,CDM}}}{dm dV} &= \frac{d^2 N_{\text{LOS,SIDM}}}{dm dV} \\ &= \delta_{\text{LOS}} (1 + \xi_{2\text{halo}}(r, M_{\text{halo}}, z)) \left[\frac{d^2 N}{dm dV} \right]_{\text{ST}}, \end{aligned} \quad (9)$$

where

$$\xi_{2\text{halo}}(r, M_{\text{halo}}, z) = b(M_{\text{halo}}, z) \xi_{\text{lin}}(r, z). \quad (10)$$

The term $\xi_{2\text{halo}}(r, M_{\text{halo}}, z)$ is determined by the halo bias $b(M_{\text{halo}}, z)$ around the parent halo with mass M_{halo} as computed in [Sheth & Tormen \(1999\)](#) and the linear matter correlation function $\xi_{\text{lin}}(r, z)$ at a distance r computed using the linear power spectrum at redshift z . Unless otherwise specified in the paper, the line-of-sight mass function normalization δ_{LOS} is set to 1.0.

2.3.2 WDM halo mass functions

As discussed in Section 2.1, free-streaming of fully thermalized WDM particles results in a strong suppression of the WDM halo abundance below the half-mode mass. As a result, over the course of this study, we employ WDM substructure and line-of-sight mass functions proposed by [Lovell \(2020\)](#), which provide a reasonable fit to the simulation results. By adopting the suppression factors, which are dependent on the halo mass and the half-mode mass, the subhalo and line-of-sight halo mass functions are then given by

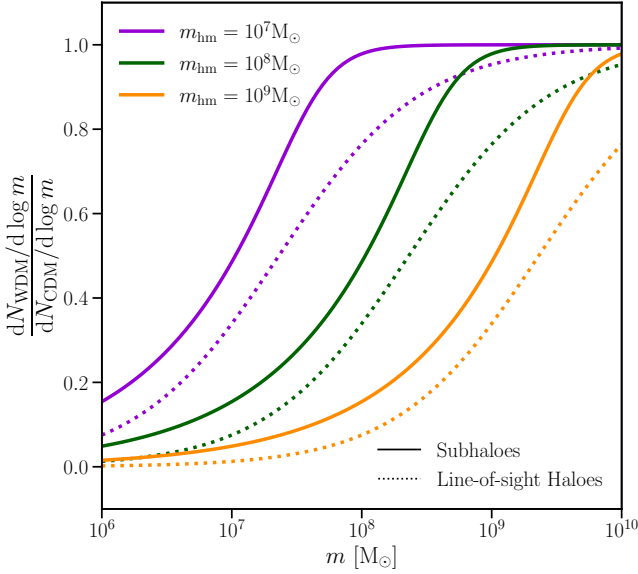


Figure 2. The ratio of WDM to CDM mass functions as a function of half-mode mass for main lens substructure (using the bound mass definition) and line-of-sight dark matter haloes (using the mass definition M_{200}).

$$\frac{dN_{\text{sub,WDM}}}{d \log m} = \frac{dN_{\text{sub,CDM}}}{d \log m} \left[1 + \left(4.2 \frac{m_{\text{hm}}}{m} \right)^{2.5} \right]^{-0.2} \quad (11)$$

and

$$\frac{dN_{\text{LOS,WDM}}}{d \log m} = \frac{dN_{\text{LOS,CDM}}}{d \log m} \left[1 + \left(2.3 \frac{m_{\text{hm}}}{m} \right)^{0.8} \right]^{-1.0}, \quad (12)$$

respectively.

The ratio of the WDM and CDM mass functions obtained by equations (11) and (12) as a function of half-mode mass (m_{hm}) for subhaloes and line-of-sight haloes is shown in Fig. 2. In comparison to the CDM model, the WDM model exhibits a substantial suppression of the number of haloes below m_{hm} due to free streaming effects. The WDM subhalo mass function turnover occurs at lower masses than the WDM line-of-sight halo mass function, which is consistent with the fact that the bound subhalo mass definition we used for substructure accounts for tidal truncation, whereas the virial mass definition, M_{200} , we use for line-of-sight haloes is unaffected by such effects.

3 EFFECTIVE MULTIPLANE LENSING AND DIFFERENT ANGULAR AND SYMMETRY STRUCTURES IN CONVERGENCE FIELDS

In this section, we look at the concept of effective multiplane gravitational lensing and the different anisotropic and symmetry structures produced by line-of-sight dark matter haloes in the divergence and the curl of the effective deflection field briefly.

3.1 Effective multiplane lensing

Photons encounter repeated deflections by dark matter haloes along the line-of-sight as they travel through the Universe from a background source to an observer. The usual method for dealing with this

multiplane gravitational lensing involves a recursive lens equation that must be solved for each lens plane (Blandford & Narayan 1986; McCully et al. 2014; Schneider 2019). This usual strategy, however, is computationally expensive.

The effective multiplane lensing approach takes into account the cumulative influence of all the lens planes in the strong lens system and reduces it to a single mapping between the observer and the source (Gilman et al. 2019, 2020a; Dhanasingham et al. 2023). The two-dimensional non-linear mapping from the source plane to the image plane in single-plane lensing is a pure gradient of a scalar lensing potential. However, due to the non-linear coupling between connective lens planes, this map no longer acts as a pure gradient of a scalar potential in the multiplane lensing phenomenon. To capture these non-linear coupling effects, the effective multiplane technique outlined in Dhanasingham et al. (2023) incorporates a curl of an effective vector potential, \mathbf{A}_{eff} , in addition to the gradient of the effective scalar potential, ϕ_{eff} , and so gives the lens equation as

$$\mathbf{u}(\mathbf{x}) = \mathbf{x} - \alpha_{\text{eff}}(\mathbf{x}), \quad (13)$$

where the "effective" deflection field $\alpha_{\text{eff}}(\mathbf{x})$ is

$$\alpha_{\text{eff}}(\mathbf{x}) = \nabla \phi_{\text{eff}}(\mathbf{x}) + \nabla \times \mathbf{A}_{\text{eff}}(\mathbf{x}). \quad (14)$$

Here, $\mathbf{u}, \mathbf{x} \in \mathbb{R}^2$ are the source and image plane coordinates, respectively. It is worth noting that the effective vector potential, \mathbf{A}_{eff} , points purely in the line-of-sight (or $\hat{\mathbf{z}}$) direction. Without any approximation, potential functions ϕ_{eff} and \mathbf{A}_{eff} encode the entire non-linear multiplane lensing map from the source plane to the image plane.

As long as the vector field α_{eff} is twice continuously differentiable, the general decomposition introduced in equation (14) follows from the Helmholtz theorem. Potentials ϕ_{eff} and \mathbf{A}_{eff} can be computed for any behaviour of the effective deflection field at large distances from the centre of the lens by including the appropriate boundary terms.

It is useful to introduce the divergence (κ_{div}) and curl (κ_{curl}) of the effective deflection field in the study of multiple gravitational lensing, so that (Gilman et al. 2019; Dhanasingham et al. 2023)

$$\kappa_{\text{div}} \equiv \frac{1}{2} \nabla \cdot \alpha_{\text{eff}} - \kappa_0, \quad (15)$$

and

$$\kappa_{\text{curl}} \equiv \frac{1}{2} \nabla \times \alpha_{\text{eff}} \cdot \hat{\mathbf{z}}. \quad (16)$$

We subtract the projected mass density of the single-plane main lens model, κ_0 , from the divergence of the effective deflection field to remove the dominant lensing contribution from the so-called macrolens. The κ_{curl} disappears in single-plane gravitational lensing because the effective deflection field is a pure gradient. Fig. 3 depicts these two quantities for a CDM model.

3.1.1 Convergence fields with different angular structures

The different angular structures present in the κ_{div} and κ_{curl} convergence fields of a CDM halo realization containing both the line-of-sight haloes and the main lens substructure are depicted in Fig. 3. According to Dhanasingham et al. (2023), line-of-sight haloes appear stretched in the angular direction and form arc-like shapes in the κ_{div} map (left panel) because their deflection field is distorted by the main lens due to the non-linear nature of multiplane lensing. In addition to the obvious break in homogeneity caused by the macrolens, these arc-like structures add anisotropic signatures to the κ_{div} map, whereas

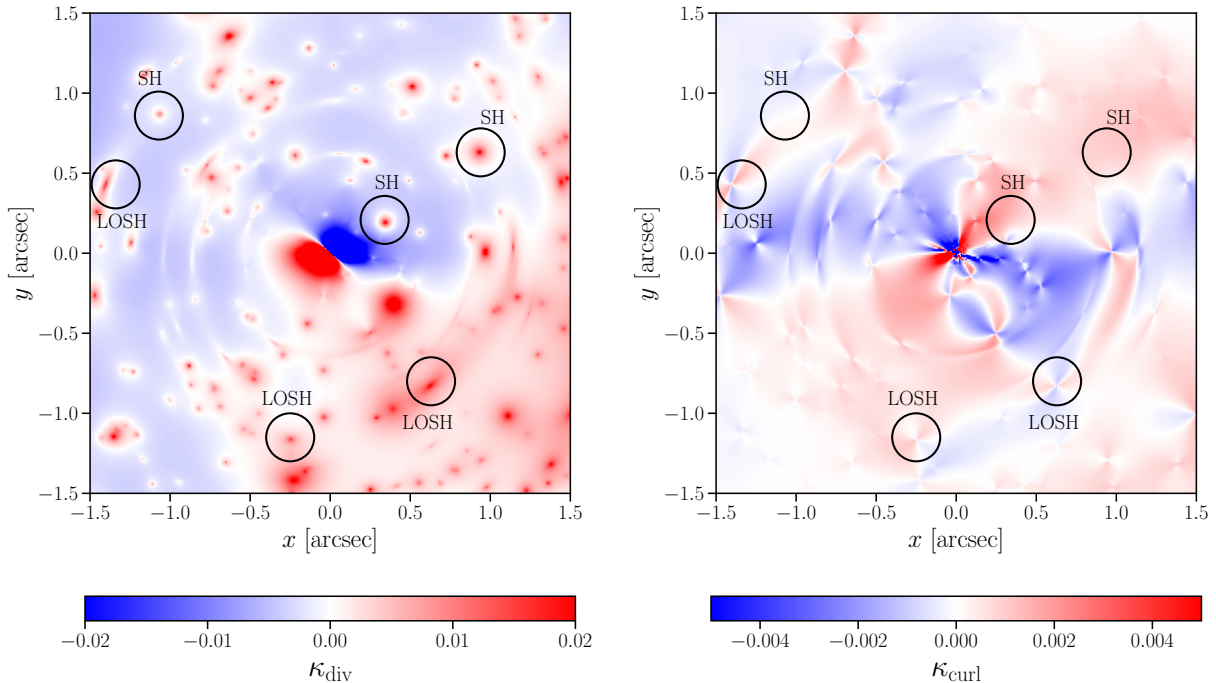


Figure 3. The κ_{div} (left panel) and κ_{curl} (right panel) convergence maps for a CDM halo realization include both the contribution from line-of-sight dark matter haloes (LOSH) and lens galaxy substructure (SH), with $(\Sigma_{\text{sub}}/\text{kpc}^{-2}, \delta_{\text{LOS}}, \log_{10}(m_{\text{min}}/M_{\odot}), \log_{10}(m_{\text{max}}/M_{\odot})) = (0.025, 1.0, 7, 10)$, taking into account the effective multiplane gravitational lensing. Take note of the varying angular structure in each case. Line-of-sight dark matter haloes seem warped in the tangential direction in the left panel, while subhaloes are usually circular. Also, line-of-sight haloes are accompanied by a quadrupolar pattern in the right panel, whereas subhaloes do not contribute to this map.

subhaloes remain largely circular and thus isotropic. Of course, due to tidal effects, main-lens subhaloes could be elliptical or stretched in specific directions, but given the projected nature of lensing, we expect the ellipticity direction from those to be random rather than preferably aligned in the angular direction. By comparing the left and right panels of Fig. 3, it is also possible to see that the stretched features in the κ_{div} map correspond to quadrupolar patterns in the κ_{curl} map. The circular features in the κ_{div} field, which correspond to subhaloes, on the other hand, are not accompanied by any specific features in the κ_{curl} map.

These apparent anisotropic signatures in the κ_{div} field and accompanying quadrupolar pattern in the κ_{curl} map, as stated by Dhanasingham et al. (2023), propose a way to distinguish between the subhaloes and line-of-sight dark matter haloes behind and in front of the main lens. In this paper, we exploit the diverse angular structures created by dark matter haloes to investigate several dark matter models.

3.1.2 Parity and *E*- and *B*-modes in effective multiplane lensing

Consider the arc-shaped structure in the κ_{div} convergence field and the accompanying quadrupole in the κ_{curl} field formed by a mass distribution along the line-of-sight. $\theta \in [0, \pi]$ is the angle measured in the clockwise direction from the centre of the projected mass density with respect to the line-of-sight, as shown in Fig. 4. Indeed, in the κ_{div} and κ_{curl} maps, these line-of-sight haloes exhibit quadrupolar patterns with two different symmetry structures.

The transformation $\theta \rightarrow -\theta$ gives $\kappa_{\text{div}}(r, -\theta) \approx \kappa_{\text{div}}(r, \theta)$ and leaves the κ_{div} unchanged (see Fig. 4). After a parity transformation, the κ_{div} is therefore locally invariant and exhibits *even* parity. As a result, in effective multiplane lensing, these tangential dis-

tortions with even parity can be introduced as “*E*-modes”. Unlike the symmetry structure of the κ_{div} map, the κ_{curl} map transforms as $\kappa_{\text{curl}}(r, -\theta) \approx -\kappa_{\text{curl}}(r, \theta)$ and thus exhibits *odd* parity under the transformation $\theta \rightarrow -\theta$. Therefore, we referred to these unique quadrupoles with odd parity as “*B*-modes”. In this paper, we combine previously unstudied parity information found in the divergence and curl components of the convergence field of a strong lens system with their unique angular structures, including quadrupoles and anisotropies, to investigate various dark matter models using the theory of effective multiplane lensing.

3.2 Quantifying anisotropies, quadrupoles, and symmetries

In this subsection, we present methods for quantifying anisotropies and quadrupoles formed by line-of-sight haloes in κ_{div} and κ_{curl} convergence fields in order to extract useful information on the dark matter microphysics of line-of-sight haloes under the effect of mass-sheet degeneracy.

3.2.1 Mass-sheet degeneracy

In general, strong lensing systems have an inherent mathematical degeneracy in which a simultaneous transformation of the source and lens planes known as the source position transform (Schneider & Sluse 2014; Unruh et al. 2017; Wertz et al. 2018) can render certain astrometric and photometric lensing observables invariant. Because we observe strong lenses in angular projection on the sky and these angles are ratios of distances, we may always rescale such distances while keeping the observed angles constant. Several lensing-related

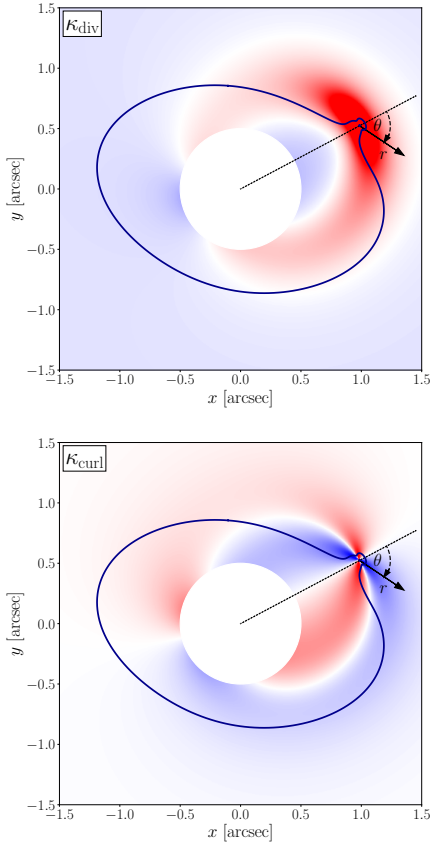


Figure 4. The distinct angular and symmetry structures are shown in the κ_{div} and κ_{curl} maps for a simple lens system with a NFW line-of-sight halo. The critical curve of the strong lens system is represented by the solid blue line.

works have addressed this mathematical degeneracy (see e.g., Schneider & Seitz 1995; Bradač et al. 2004; Schneider & Sluse 2013; Rexroth et al. 2016; Birrer 2021; Cremonese et al. 2021; Dhanasingham et al. 2023), and this can be broken only by observations on an absolute scale, such as the inherent size of the lensed source or the relative time delay between lensed images.

The well-known mass-sheet degeneracy (Falco et al. 1985) is the scalar portion of this transformation. The mass-sheet transform (MST) converts the effective deflection field as:

$$\alpha'_{\text{eff}}(\mathbf{x}) = \lambda \alpha_{\text{eff}}(\mathbf{x}) + (1 - \lambda) \mathbf{x} \quad (17)$$

by isotropically mapping the source plane coordinates as $\mathbf{u} \rightarrow \lambda \mathbf{u}$. For this mapping, the effective convergence field, $\kappa_{\text{eff}} = \frac{1}{2} \nabla \cdot \alpha_{\text{eff}}$, can be rescaled as:

$$\kappa'_{\text{eff}}(\mathbf{x}) = \lambda \kappa_{\text{eff}}(\mathbf{x}) + (1 - \lambda). \quad (18)$$

We may then write down the transformation of the κ_{div} field under MST as:

$$\kappa'_{\text{div}} = \lambda \kappa_{\text{div}} \quad (19)$$

using the MST of the macrolens convergence field, $\kappa'_0(\mathbf{x}) = \lambda \kappa_0(\mathbf{x}) + (1 - \lambda)$. Similarly, we may rescale the κ_{curl} field as:

$$\kappa'_{\text{curl}} = \lambda \kappa_{\text{curl}} \quad (20)$$

by considering the curl of the effective deflection field provided in equation (17). Therefore, MST scales the two-point correlation function of a given convergence field as $\xi(\mathbf{r}) \rightarrow \lambda^2 \xi(\mathbf{r})$, and thereby

biases its amplitude by a factor of λ^2 . Dhanasingham et al. (2023) used a normalized two-point correlation function approach to eliminate the effects of mass-sheet degeneracy, but for simplicity, we do not consider this normalization here because we are primarily interested in the overall shape of the two-point correlation function. Nonetheless, this normalization factor could be trivially restored to remove the impact of the MST.

3.2.2 The two-point correlation function

As stated in Dhanasingham et al. (2023), the contribution of the line-of-sight halo to the convergence field κ_{div} is no longer statistically isotropic, and there are also interesting quadrupole structures at the positions of the line-of-sight haloes present in the convergence field κ_{curl} . To capture the fruitful information encoded in these anisotropies and quadrupole structures, we employ the image plane-averaged two-point correlation function, denoted as:

$$\xi(\mathbf{r}) = \frac{1}{A} \int_A d^2 \mathbf{r}_1 [\kappa(\mathbf{r}_1) - \langle \kappa(\mathbf{r}_1) \rangle] [\kappa(\mathbf{r}_2) - \langle \kappa(\mathbf{r}_2) \rangle], \quad (21)$$

where \mathbf{r}_1 and $\mathbf{r}_2 = \mathbf{r}_1 + \mathbf{r}$ are the position vectors of two points from the center of the convergence field, \mathbf{r} is the vector linking these two points, and A is the area of the image where the spatial average is performed. Here, κ represents either κ_{div} or κ_{curl} and $\langle \kappa(\mathbf{r}) \rangle$ is the mean of the convergence map.

On the convergence map, we use a binary annular mask with the region of interest set to 1 and the domain to be masked out set to 0 to focus our attention on the relevant region close to the Einstein radius of the main lens. Using the point-wise multiplications of masks, $W(\mathbf{r})$, and convergence maps such that $\tilde{\kappa}(\mathbf{r}) = W(\mathbf{r}) \cdot \kappa(\mathbf{r})$, the masked correlation function of the convergence overdensity field (see e.g., Padfield 2010, 2012; Dhanasingham et al. 2023, for similar works) can be written as:

$$\xi(\mathbf{r}) = \frac{1}{A} \int d^2 \mathbf{r}_1 \tilde{\kappa}(\mathbf{r}_1) \tilde{\kappa}(\mathbf{r} + \mathbf{r}_1) - \frac{\int d^2 \mathbf{r}_1 \tilde{\kappa}(\mathbf{r}_1) W(\mathbf{r} + \mathbf{r}_1) \cdot \int d^2 \mathbf{r}_1 W(\mathbf{r}_1) \tilde{\kappa}(\mathbf{r} + \mathbf{r}_1)}{A \int d^2 \mathbf{r}_1 W(\mathbf{r}_1) W(\mathbf{r} + \mathbf{r}_1)}. \quad (22)$$

3.2.3 Decomposing the two-point function of κ_{div} field

The distortions of the projected mass density of line-of-sight haloes in the tangential direction exhibit quadrupoles with even parity, as detailed in Section 3.1.2. We decompose the two-point function of κ_{div} onto an orthonormal basis of Chebyshev polynomials, $T_\ell(\cos \theta) = \cos(\ell \theta)$, as:

$$\xi_{\text{div}}(\mathbf{r}) = \xi_{\text{div}}(r, \theta) = \sum_{\ell=0}^{\infty} \xi_{\text{div},\ell}(r) \cos(\ell \theta), \quad (23)$$

to characterize the significant information hidden in these anisotropies together with their even parity. Here θ is the angle between \mathbf{r} and the line-of-sight vector from the centre to the mid-point of the vector \mathbf{r} . In equation (23), the term $\xi_{\text{div},\ell}(r)$ denotes the correlation multipole of order ℓ , which is thus given by

$$\xi_{\text{div},\ell}(r) = \frac{2 - \delta_{\ell 0}}{\pi} \int_0^\pi d\theta \xi_{\text{div}}(r, \theta) \cos(\ell \theta), \quad (24)$$

where δ_{ij} is the Kronecker delta.

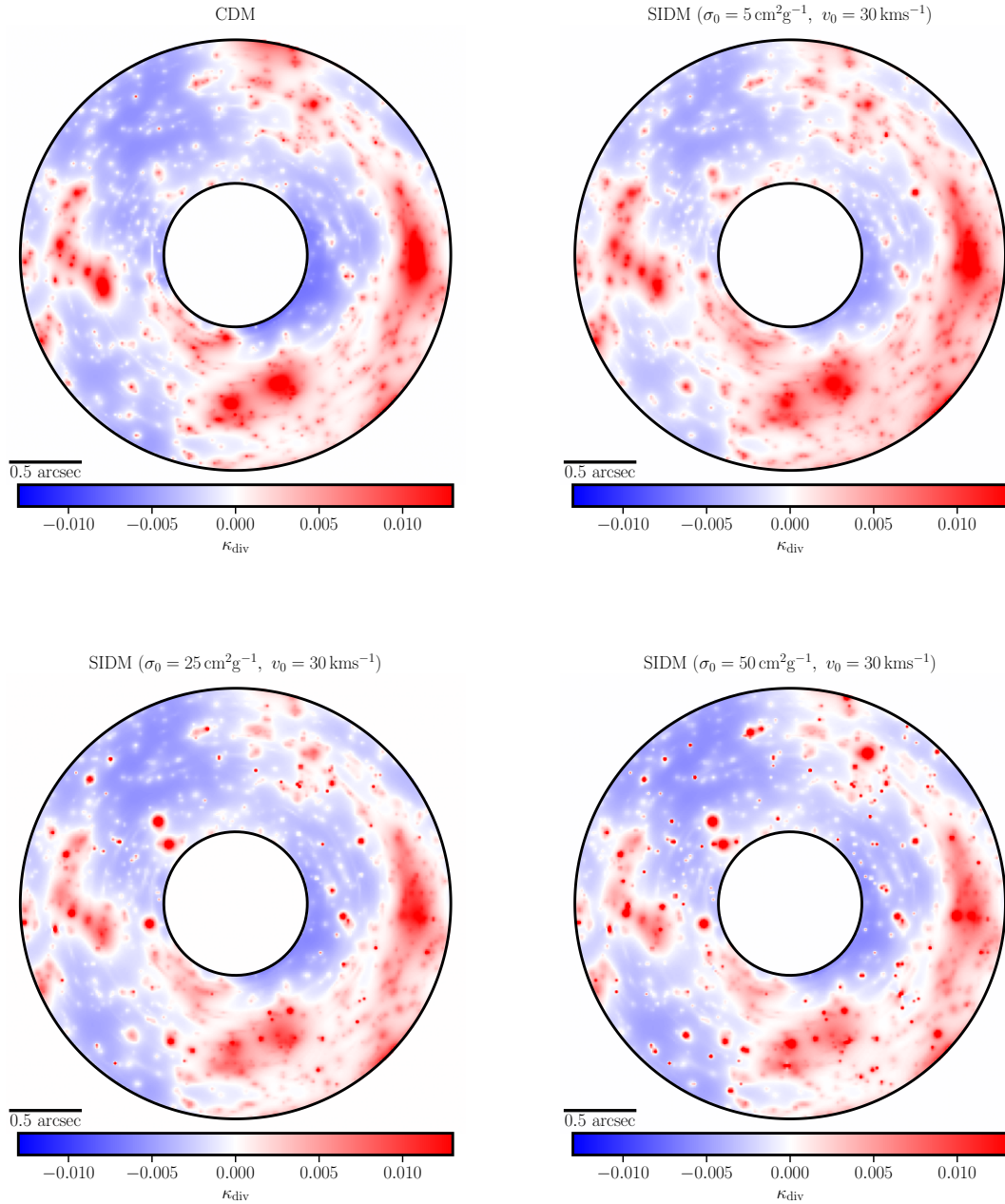


Figure 5. The κ_{div} convergence maps for three SIDM models with different interaction cross-sections and a CDM realization take into account both the contribution from the main lens substructure and line-of-sight haloes. As the cross-section increases, the number of core-collapsed subhaloes and line-of-sight haloes increases, resulting in high-density peaks on the convergence maps.

3.2.4 Decomposing the two-point function of κ_{curl} field

As mentioned in Section 3.1.2, the quadrupole structures in the κ_{curl} field have a unique symmetry structure with odd parity. Therefore, it is useful to introduce a set of orthonormal basis functions, $\{A_\theta \sin(\ell\theta)\}$, to decompose the two-point correlation function, $\xi_{\text{curl}}(\mathbf{r})$, by taking into account the odd-parity of these quadrupole structures in order to extract useful information from the convergence field κ_{curl} about the small-scale dark matter structure along the line-of-sight of the observer and the source. Then we can write down the

two-point function as:

$$\xi_{\text{curl}}(\mathbf{r}) = \xi_{\text{curl}}(r, \theta) = \sum_{\ell=1}^{\infty} \xi_{\text{curl},\ell}(r) A_\theta \sin(\ell\theta), \quad (25)$$

where the parameter

$$A_\theta = \begin{cases} +1 & 0 \leq \theta < \frac{\pi}{2}, \\ -1 & \frac{\pi}{2} \leq \theta < \pi, \end{cases} \quad (26)$$

is used to extract the useful information hidden in the previously mentioned odd parity structure. The basis functions we introduced here satisfy the following orthogonality condition:

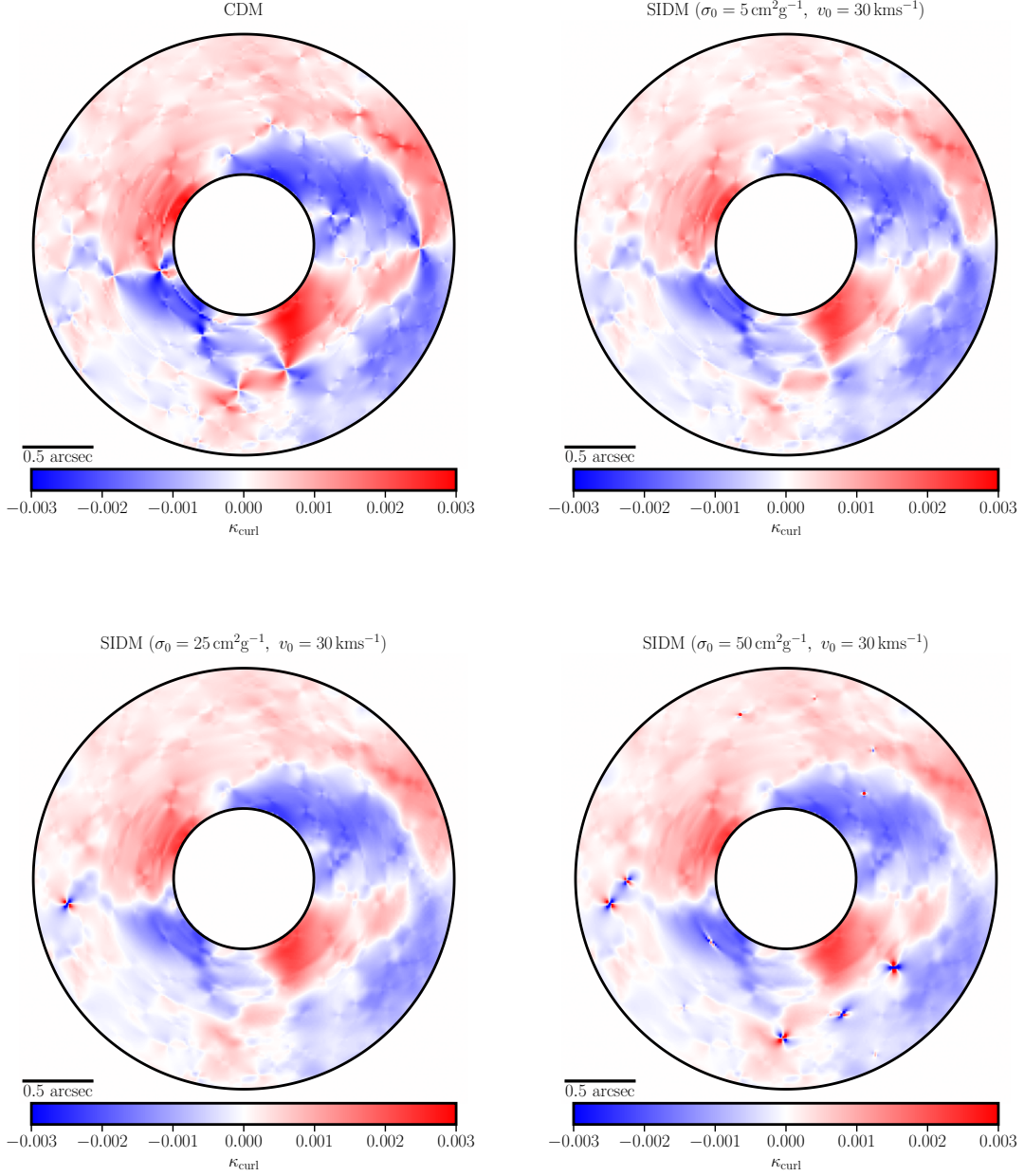


Figure 6. The κ_{curl} convergence maps for SIDM and CDM models shown in Fig. 5. Only line-of-sight haloes contribute to these maps, and steep density cusps of core-collapsed such haloes imprint conspicuous quadrupole patterns in the convergence fields of SIDM realizations.

$$\int_0^\pi d\theta A_\theta \sin(\ell\theta) A_\theta \sin(m\theta) = \int_0^\pi d\theta \sin(\ell\theta) \sin(m\theta) = \frac{\pi}{2} \delta_{\ell m}, \quad (27)$$

where $\delta_{\ell m}$ is the Kronecker delta. Using these relations, the corresponding correlation multipoles of order ℓ can be written as

$$\xi_{\text{curl},\ell}(r) = \frac{2}{\pi} \int_0^\pi d\theta \xi_{\text{curl}}(r, \theta) A_\theta \sin(\ell\theta). \quad (28)$$

4 RESULTS

In this section, we will look at the anisotropies that emerge in the κ_{div} and κ_{curl} maps, focusing on SIDM and WDM theories while utilizing the typical CDM model as a reference. We build our dark matter realizations using the mass function and density profile options described in Section 2.

4.1 SIDM

Fig. 5 depicts the two-dimensional projected mass density field, κ_{div} , using three SIDM models with $\sigma_0 = 5, 25, 50 \text{ cm}^2 \text{ g}^{-1}$ and $v_0 = 30 \text{ km s}^{-1}$, with the CDM model serving as the reference. When the velocity-dependent interaction cross-section is increased, more

SIDM substructure and line-of-sight haloes begin to form cores and become less dense. As we further increase the cross-section these haloes begin to core-collapse, resulting in high-density peaks on these maps. The top-right panel of Fig. 5 contains a small number of core-collapsed subhaloes and zero core-collapsed line-of-sight haloes, whereas the bottom-right panel contains more core-collapsed line-of-sight dark matter haloes represented by dense structure stretched in the tangential direction, in addition to a relatively larger number of core-collapsed subhaloes appearing as dense circular structure. Fig. 6 illustrates the κ_{curl} field of the same SIDM and CDM models. The quadrupolar pattern at the places of line-of-sight haloes distinguishes these maps. When compared to the CDM model and SIDM models with small velocity-dependent cross-sections, the SIDM models with large cross-sections imprint more pronounced quadrupole patterns due to the steep density cusps of core-collapsed line-of-sight dark matter haloes. Furthermore, for large cross-sections, the large-scale features are obviously getting more diffuse, even as the small haloes begin core-collapsing. When compared to CDM haloes with cuspy density profiles, the low central density of cored SIDM substructure and line-of-sight haloes contribute to the convergence maps with faint features in both Figs. 5 and 6.

The monopole and quadrupole moments of the two-point function, ξ_{div} , as well as the quadrupole moments of the two-point correlation function, ξ_{curl} , are shown in Fig. 7 for three different SIDM models with velocity-dependent self-interaction cross-section normalization (σ_0) values of 5, 25, 50 cm^2g^{-1} and $v_0 = 30 \text{ km s}^{-1}$, and the CDM model as the benchmark. These plots have been made using 100 different realizations for each dark matter model. The lines reflect the mean, and the dark and light-shaded regions represent 68 and 90 per cent credible intervals, respectively. Due to the shallow density cores and the relatively small number of core-collapsed haloes, the SIDM model with the smallest cross-section has a lower relative amplitude compared to the CDM model in all three panels of Fig. 7. In comparison, the SIDM model with $\sigma_0 = 25 \text{ cm}^2\text{g}^{-1}$ has a large number of core-collapsed subhaloes and a small number of core-collapsed line-of-sight haloes. This core-collapsed substructure significantly contributes to the increase in the amplitude of the monopole of the ξ_{div} function, while the presence of mostly cored line-of-sight haloes slightly decreases its quadrupole moment compared to the CDM case. Meanwhile, the very small number of core-collapsed line-of-sight haloes in this case slightly increases the quadrupole moment of the ξ_{curl} function on small scales.

The SIDM model with the largest cross-section produces a significant number of core-collapsed line-of-sight haloes in addition to the core-collapsed substructure, which contributes significantly to the large amplitude of the monopole of the ξ_{div} function and the quadrupole of the ξ_{curl} function, which purely represent the line-of-sight haloes. More interestingly, we can see a large relative amplitude of the quadrupole of the ξ_{div} function at small radial distances compared to the SIDM models with small cross-sections due to the significant number of core-collapsed line-of-sight haloes. At small radial distances, this increase in amplitude is accompanied by a steepening of the slope of $\xi_{\text{div},2}(r)$, reflecting the steeper density profile of collapsed line-of-sight haloes. However, at large radial distances, the cored SIDM line-of-sight haloes dominate the amplitude of this quadrupole moment, resulting in a modest relative amplitude compared to the other three models. One of the most apparent features of all three panels is that when moving toward large angular separations, all shown correlation functions for the different models considered asymptote to the same behaviour, echoing the fact that SIDM does not significantly alter the outskirts of dark matter haloes.

The influence of the characteristic velocity, v_0 , contained in the

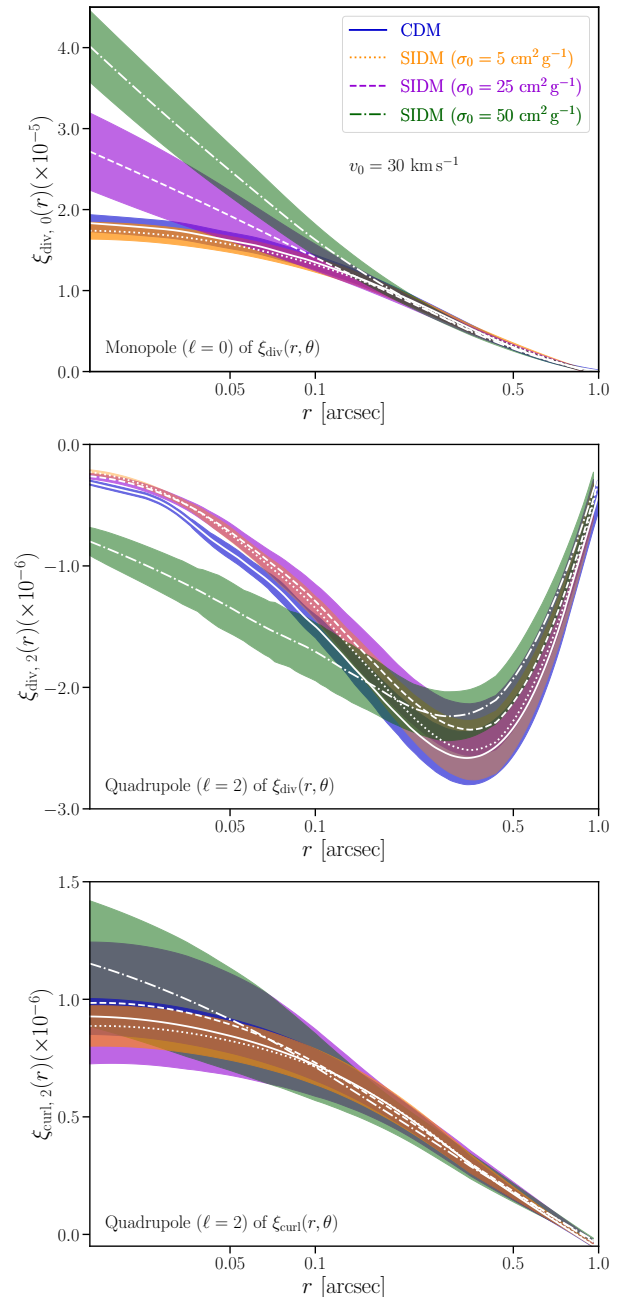


Figure 7. The monopole (top panel) and the quadrupole (middle panel) moments of the two-point function ξ_{div} , and the quadrupole (bottom panel) moment of ξ_{curl} function as a function of the velocity-dependent interaction cross-section normalization (σ_0) for three SIDM models. The CDM model serves as the reference point in this case. All three panels in this narrative have the same legend. The 68% credible intervals are shown in the shaded areas. The amplitudes of multipoles are primarily determined by the density profile shape and the abundance of cored and core-collapsed haloes.

velocity-dependent cross-section on the multipole moments of the two-point functions ξ_{div} and ξ_{curl} is seen in Fig. 8. As expected, the relative amplitudes of the quadrupole moments of these two-point functions decrease as the interaction cross-section grows. This reflects the presence of a larger core in more massive line-of-sight haloes and subhaloes as v_0 is increased. Furthermore, when v_0 grows the amplitude of the ξ_{div} monopole initially reduces (reflecting core

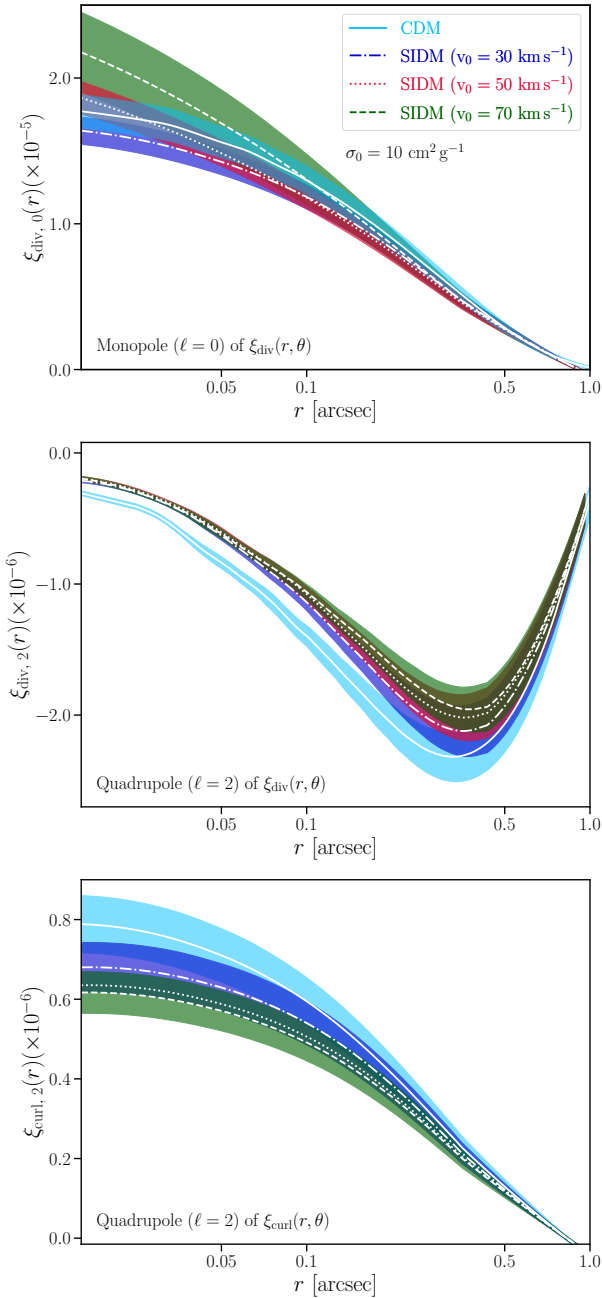


Figure 8. The same as in Fig. 7, but this time as a function of the characteristic velocity (v_0).

formation) and subsequently increases in comparison to the benchmark CDM model (reflecting the presence of core-collapsed subhaloes for the $v_0 = 70 \text{ km s}^{-1}$ case).

The relative differences between the two-point correlation function multipoles of the SIDM models we reviewed here and the CDM model are shown in Figs. B1 and B2 in Appendix B. In all, we see that the *combination* of the monopole and quadrupole moments of the ξ_{div} correlation function contains important information about both the amplitude of the self-interaction cross-section at low velocities and about its characteristic velocity. For instance, a steepening of the $\xi_{\text{div},0}$ moment without an accompanied increase in the amplitude of the $\xi_{\text{div},2}$ moment indicates a self-interaction cross-section

large enough to core-collapse subhaloes but not line-of-sight haloes, while an increase in both indicates a cross-section large enough to collapse all haloes, whether or not they are in the tidal field of a host. Furthermore, the exact shape of the steepened $\xi_{\text{div},0}$ moment can tell us about the velocity dependence of the cross-section since it reflects which subhalo masses have large cores, which are core-collapsed, and which ones are largely unaffected by self-interaction.

4.2 WDM

The monopole and quadrupole moments of the two-point function ξ_{div} , as well as the quadrupole moment of the ξ_{curl} function, are shown in Fig. 9 for three different WDM models with various half-mode masses (m_{hm}). The WDM particle mass ($m_{\text{WDM}} \sim 4.5 \text{ keV}$) obtained by Villaseñor et al. (2023) using Lyman- α flux power spectrum data corresponds to $m_{\text{hm}} \simeq 10^8 M_{\odot}$ line in Fig. 9. As the half-mode mass increases, the number of substructure and line-of-sight haloes decreases, and the central densities of such WDM haloes are relatively suppressed compared to CDM haloes of the same mass due to their lower concentrations. Because the amplitudes of two-point function multipoles are sensitive to the central density of dark matter haloes, particularly at small radial distances, the suppression of halo concentrations for masses below m_{hm} produces smaller perturbations to the lensed images than CDM haloes, and thus the anisotropic signal imprinted by line-of-sight dark matter haloes is low. Therefore these effects can be seen as a progressive decrease in the relative amplitude of the multipoles with respect to the CDM model as the half-mode mass increases.

For small radial distances, the amplitude of the different multipole moments diminishes as the half-mode mass grows. This reflects the suppressed abundance of small haloes, which are the primary contributors to the correlation function at these scales. At large radial distances, the correlation functions for the different models shown converge to the same behaviour because the abundance of large haloes (which dominate at these scales) is essentially unaffected by these free-streaming effects.

5 DISCUSSION AND CONCLUSIONS

In this work, we have investigated how the two-point correlation function of the κ_{div} field of dark matter haloes in a strong lens system evolves when both self-interacting and warm dark matter scenarios are considered while maintaining the cold dark matter framework as the benchmark. We were particularly interested in the parity-even quadrupole moment of this two-point function, which is produced by the anisotropic fingerprints generated by line-of-sight dark matter haloes due to non-linear coupling between various lens planes. We also developed a framework for computing the parity-odd quadrupole moment of the κ_{curl} field's two-point function, which only arises in the presence of line-of-sight dark matter haloes. We investigated how the correlation function multipoles behave as a function of the self-interaction cross-section in the SIDM scenario, which essentially dictates the abundance and density profiles of cored or core-collapsed haloes in a strong lens system. Our results can be summarized as follows:

- For small values of the cross-section, cored haloes dominate the amplitudes of the monopole and quadrupole of the two-point function of the κ_{div} field, resulting in a reduced relative amplitude compared to the CDM scenario.

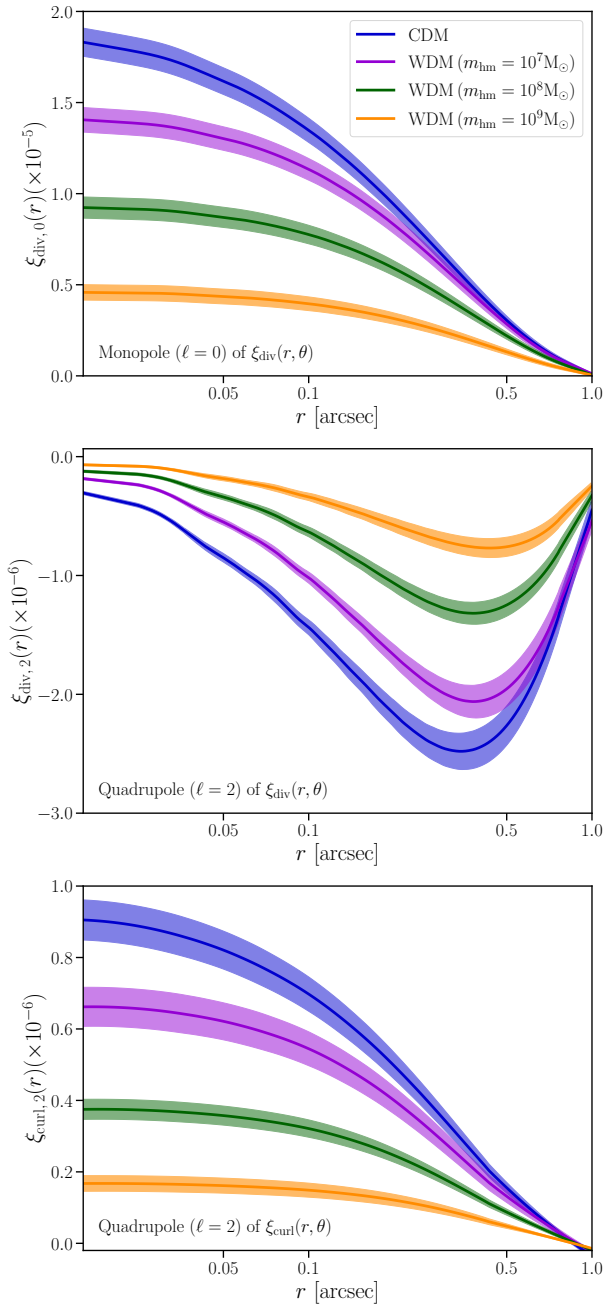


Figure 9. The monopole (top panel) and the quadrupole (middle panel) moments of the two-point function ξ_{div} , and the quadrupole (bottom panel) of the function ξ_{curl} as a function of half-mode mass (m_{hm}) for three WDM models. The CDM model serves as the benchmark in this case. All three panels in this plot have the same legend. The 68% credible intervals are shown in the shaded areas. The abundance and concentration of subhaloes and line-of-sight dark matter haloes have the greatest influence on multipole amplitudes.

- As the self-interaction cross-section grows, subhaloes can begin to core-collapse, resulting in a steeper and larger monopole at small radial distances. Meanwhile, line-of-sight haloes, which are not subjected to tidal truncation, are still in the cored density profile regime, resulting in a relatively suppressed quadrupole moment of the κ_{div} field as compared to the CDM case.

- As the self-interaction cross-section grows further, both sub-

haloes and line-of-sight haloes undergo core collapse, resulting in both the monopole and quadrupole of the ξ_{div} correlation function becoming large and steep at small radial distances. In parallel, the parity-odd (curl) quadrupole correlation function displays a slight increase in amplitude at small radial distances due to the core-collapsed line-of-sight haloes.

- For large enough self-interaction cross-section, the exact slope of the monopole and quadrupole of the ξ_{div} correlation function at small radial distances depends on the characteristic velocity v_0 .

It is thus clear that using detailed observations with high signal-to-noise ratio and resolution, both the monopole and quadrupole moments of the ξ_{div} correlation function, especially at small radial distances, could constrain both the amplitude and velocity dependence of the SIDM cross-section.

In the WDM scenario, we investigated the change in amplitudes of the two-point function multipoles as a function of the WDM’s characteristic half-mode mass, which controls the abundance of small dark matter haloes. In this case, the relative amplitudes of the different multipoles are mostly determined by the abundance of low-mass haloes. As a result, when the half-mode mass increases, the number of small haloes reduces, as do the amplitudes of the multipole moments at small radial separation.

In conclusion, based on the shapes and amplitudes of the two-point function multipoles in the two different dark matter scenarios we considered, our work shows that extracting these multipole moment signals from galaxy–galaxy strong lens observations is a promising technique for studying dark matter physics. However, a detailed study is needed to determine how well this anisotropic signal could be extracted from realistic strong lenses. Encouragingly, [Dhanasingham et al. \(2023\)](#) showed that both the monopole and quadrupole of the ξ_{div} correlation function could be jointly extracted from high-resolution mock observations of a galaxy-scale Einstein ring. Future work is needed to assess the power of a large sample of strong lenses to constrain the SIDM cross-section and the abundance of small-mass haloes via the key anisotropic signatures we have pointed out in this work. With upcoming space- and ground-based surveys in this decade to observe and detect strong lens systems ([Serjeant 2014](#); [Collett 2015](#); [Serjeant 2017](#); [Metcalf et al. 2019](#); [Weiner et al. 2020](#); [Mao et al. 2022](#)), such a study will help us better grasp the dark Universe.

ACKNOWLEDGEMENTS

We would like to express our gratitude to the anonymous referee for providing insightful comments and suggestions on this manuscript for improvements. We would also like to thank Tansu Daylan, Daniel Gilman, Xiaolong Du, Carton Zeng, Ekapob Kulchoakrungsun, Ky-lar L. Greene, David Camarena, and Soumyodipta Karmakar for useful discussions. B.D. and F.-Y.C.-R. acknowledge the support of program HST-AR-17061.001-A whose support was provided by the National Aeronautical and Space Administration (NASA) through a grant from the Space Telescope Science Institute, which is operated by the Association of Universities for Research in Astronomy, Incorporated, under NASA contract NAS5-26555. This work was supported in part by the NASA Astrophysics Theory Program under grant 80NSSC18K1014. F.-Y. C.-R. would like to thank the Robert E. Young Origins of the Universe Chair fund for its generous support. We also would like to thank the UNM Center for Advanced Research Computing, supported in part by the National Science Foundation, for providing the high-performance computing resources used in this work. B. D. would like to thank Kevin Fotso Tagne and Bhashithe

Abeyasinghe for their assistance with high-performance computing. The work in this manuscript made partial use of the PYTHON packages NUMPY (Harris et al. 2020), NUMBA (Lam et al. 2015), MATPLOTLIB (Hunter 2007), SCIPY (Virtanen et al. 2020), ASTROPY (Astropy Collaboration et al. 2018), and COLOSSUS (Diemer 2018). We are appreciative of the great work done by the developers of these software.

DATA AVAILABILITY

All the data generated in this research, as well as the codes used, will be available upon reasonable request to the corresponding author.

REFERENCES

- Adam A., Perreault-Levasseur L., Hezaveh Y., Welling M., 2023, *arXiv e-prints*, p. [arXiv:2301.04168](https://arxiv.org/abs/2301.04168)
- Ahn K.-J., Shapiro P. R., 2005, *MNRAS*, 363, 1092
- Amorisco N. C., et al., 2022, *MNRAS*, 510, 2464
- Andrade K. E., Fuson J., Gad-Nasr S., Kong D., Minor Q., Roberts M. G., Kaplinghat M., 2022, *MNRAS*, 510, 54
- Astropy Collaboration et al., 2018, *AJ*, 156, 123
- Auger M. W., Treu T., Bolton A. S., Gavazzi R., Koopmans L. V. E., Marshall P. J., Bundy K., Moustakas L. A., 2009, *ApJ*, 705, 1099
- Auger M. W., Treu T., Bolton A. S., Gavazzi R., Koopmans L. V. E., Marshall P. J., Moustakas L. A., Burles S., 2010, *ApJ*, 724, 511
- Balberg S., Shapiro S. L., 2002, *Phys. Rev. Lett.*, 88, 101301
- Balberg S., Shapiro S. L., Inagaki S., 2002, *ApJ*, 568, 475
- Baltz E. A., Marshall P., Oguri M., 2009, *J. Cosmology Astropart. Phys.*, 2009, 015
- Banerjee A., Adhikari S., Dalal N., More S., Kravtsov A., 2020, *J. Cosmology Astropart. Phys.*, 2020, 024
- Bayer D., Chatterjee S., Koopmans L. V. E., Vegetti S., McKean J. P., Treu T., Fassnacht C. D., Glazebrook K., 2023a, *MNRAS*, 523, 1310
- Bayer D., Koopmans L. V. E., McKean J. P., Vegetti S., Treu T., Fassnacht C. D., Glazebrook K., 2023b, *MNRAS*, 523, 1326
- Benson A. J., 2012, *New Astron.*, 17, 175
- Benson A. J., 2020, *MNRAS*, 493, 1268
- Benson A. J., et al., 2013, *MNRAS*, 428, 1774
- Birrer S., 2021, *ApJ*, 919, 38
- Birrer S., Amara A., 2018, *Physics of the Dark Universe*, 22, 189
- Birrer S., et al., 2019, *MNRAS*, 484, 4726
- Birrer S., et al., 2021, *Journal of Open Source Software*, 6, 3283
- Blandford R., Narayan R., 1986, *ApJ*, 310, 568
- Bode P., Ostriker J. P., Turok N., 2001, *ApJ*, 556, 93
- Bolton A. S., Burles S., Koopmans L. V. E., Treu T., Moustakas L. A., 2006, *ApJ*, 638, 703
- Bolton A. S., Burles S., Koopmans L. V. E., Treu T., Gavazzi R., Moustakas L. A., Wayth R., Schlegel D. J., 2008, *ApJ*, 682, 964
- Bond J. R., Szalay A. S., 1983, *ApJ*, 274, 443
- Bose S., Hellwing W. A., Frenk C. S., Jenkins A., Lovell M. R., Helly J. C., Li B., 2016, *MNRAS*, 455, 318
- Bradač M., Lombardi M., Schneider P., 2004, *A&A*, 424, 13
- Brennan S., Benson A. J., Cyr-Racine F.-Y., Keeton C. R., Moustakas L. A., Pullen A. R., 2019, *MNRAS*, 488, 5085
- Brownstein J. R., et al., 2012, *ApJ*, 744, 41
- Bullock J. S., Boylan-Kolchin M., 2017, *Ann. Rev. Astron. Astrophys.*, 55, 343
- Burger J. D., Zavala J., 2019, *MNRAS*, 485, 1008
- Canameras R., et al., 2023, *arXiv e-prints*, p. [arXiv:2306.03136](https://arxiv.org/abs/2306.03136)
- Chatterjee S., Koopmans L. V. E., 2018, *MNRAS*, 474, 1762
- Cheng T.-Y., Li N., Conselice C. J., Aragón-Salamanca A., Dye S., Metcalf R. B., 2020, *MNRAS*, 494, 3750
- Chiba M., 2002, *ApJ*, 565, 17
- Collett T. E., 2015, *ApJ*, 811, 20
- Cooray A., Hu W., 2002, *ApJ*, 574, 19
- Cooray A., Kamionkowski M., Caldwell R. R., 2005, *Phys. Rev. D*, 71, 123527
- Cornachione M. A., et al., 2018, *ApJ*, 853, 148
- Correa C. A., 2021, *MNRAS*, 503, 920
- Cremonese P., Ezquiaga J. M., Salzano V., 2021, *Phys. Rev. D*, 104, 023503
- Cross D., et al., 2023, *arXiv e-prints*, p. [arXiv:2304.10128](https://arxiv.org/abs/2304.10128)
- Cyr-Racine F.-Y., Keeton C. R., Moustakas L. A., 2019, *Phys. Rev. D*, 100, 023013
- Dalal N., Kochanek C. S., 2002, *ApJ*, 572, 25
- Dalcanton J. J., Hogan C. J., 2001, *ApJ*, 561, 35
- Dhanasingham B., Cyr-Racine F.-Y., Peter A. H. G., Benson A., Gilman D., 2023, *MNRAS*, 518, 5843
- Díaz Rivero A., Cyr-Racine F.-Y., Dvorkin C., 2018a, *Phys. Rev. D*, 97, 023001
- Díaz Rivero A., Dvorkin C., Cyr-Racine F.-Y., Zavala J., Vogelsberger M., 2018b, *Phys. Rev. D*, 98, 103517
- Diemer B., 2018, *ApJS*, 239, 35
- Diemer B., Joyce M., 2019, *ApJ*, 871, 168
- Eckert D., Eitton S., Robertson A., Massey R., Pointecouteau E., Harvey D., McCarthy I. G., 2022, *A&A*, 666, A41
- Elbert O. D., Bullock J. S., Garrison-Kimmel S., Rocha M., Oñorbe J., Peter A. H. G., 2015, *MNRAS*, 453, 29
- Falco E. E., Gorenstein M. V., Shapiro I. I., 1985, *ApJ*, 289, L1
- Gavazzi R., Treu T., Koopmans L. V. E., Bolton A. S., Moustakas L. A., Burles S., Marshall P. J., 2008, *ApJ*, 677, 1046
- Gilman D., Birrer S., Treu T., Nierenberg A., Benson A., 2019, *MNRAS*, 487, 5721
- Gilman D., Birrer S., Nierenberg A., Treu T., Du X., Benson A., 2020a, *MNRAS*, 491, 6077
- Gilman D., Du X., Benson A., Birrer S., Nierenberg A., Treu T., 2020b, *MNRAS*, 492, L12
- Gilman D., Bovy J., Treu T., Nierenberg A., Birrer S., Benson A., Sameie O., 2021, *MNRAS*, 507, 2432
- Harris C. R., et al., 2020, *Nature*, 585, 357
- Hezaveh Y. D., et al., 2016a, *ApJ*, 823, 37
- Hezaveh Y., Dalal N., Holder G., Kisner T., Kuhlen M., Perreault Levasseur L., 2016b, *J. Cosmology Astropart. Phys.*, 1611, 048
- Hezaveh Y. D., Perreault Levasseur L., Marshall P. J., 2017, *Nature*, 548, 555
- Hirata C. M., Seljak U., 2003, *Phys. Rev. D*, 68, 083002
- Hogg N. B., Fleury P., Larena J., Martinelli M., 2023, *MNRAS*, 520, 5982
- Hunter J. D., 2007, *Computing in Science & Engineering*, 9, 90
- Kahlhoefer F., Kaplinghat M., Slatyer T. R., Wu C.-L., 2019, *J. Cosmology Astropart. Phys.*, 2019, 010
- Kaplinghat M., Tulin S., Yu H.-B., 2013, *arXiv e-prints*, p. [arXiv:1308.0618](https://arxiv.org/abs/1308.0618)
- Kaplinghat M., Tulin S., Yu H.-B., 2014a, *Phys. Rev. D*, 89, 035009
- Kaplinghat M., Keeley R. E., Linden T., Yu H.-B., 2014b, *Phys. Rev. Lett.*, 113, 021302
- Kaplinghat M., Tulin S., Yu H.-B., 2016, *Phys. Rev. Lett.*, 116, 041302
- Keeley R. E., Nierenberg A. M., Gilman D., Birrer S., Benson A., Treu T., 2023, *MNRAS*, 524, 6159
- Keeton C. R., 2003, *ApJ*, 584, 664
- Kim S. Y., Peter A. H. G., Wittman D., 2017, *MNRAS*, 469, 1414
- Kochanek C. S., Dalal N., 2003, in Holt S. H., Reynolds C. S., eds, *American Institute of Physics Conference Series Vol. 666, The Emergence of Cosmic Structure*. pp 103–112 ([arXiv:astro-ph/0212274](https://arxiv.org/abs/astro-ph/0212274)), doi:10.1063/1.1581778
- Kochanek C. S., Dalal N., 2004, *ApJ*, 610, 69
- Koopmans L. V. E., 2005, *MNRAS*, 363, 1136
- Lam S. K., Pitrou A., Seibert S., 2015, in *Proc. Second Workshop on the LLVM Compiler Infrastructure in HPC*. pp 1–6, doi:10.1145/2833157.2833162
- Laroche A., Gilman D., Li X., Bovy J., Du X., 2022, *MNRAS*, 517, 1867
- Lazar A., Bullock J. S., Boylan-Kolchin M., Feldmann R., Çatmabacak O., Moustakas L., 2021, *MNRAS*, 502, 6064
- Legin R., Stone C. J., Hezaveh Y., Perreault-Levasseur L., 2022, in *Machine Learning for Astrophysics*. p. 47 ([arXiv:2207.04123](https://arxiv.org/abs/2207.04123)), doi:10.48550/arXiv.2207.04123
- Lemon C., et al., 2020, *MNRAS*, 494, 3491
- Li R., Frenk C. S., Cole S., Wang Q., Gao L., 2017, *MNRAS*, 468, 1426

- Li R., et al., 2020, *ApJ*, **899**, 30
- Lovell M. R., 2020, *ApJ*, **897**, 147
- Lynden-Bell D., Wood R., 1968, *MNRAS*, **138**, 495
- Macciò A. V., Paduroiu S., Anderhalden D., Schneider A., Moore B., 2012, *MNRAS*, **424**, 1105
- Mao S., Schneider P., 1998, *MNRAS*, **295**, 587
- Mao Y.-Y., et al., 2022, *arXiv e-prints*, p. [arXiv:2203.07252](https://arxiv.org/abs/2203.07252)
- McCully C., Keeton C. R., Wong K. C., Zabludoff A. I., 2014, *MNRAS*, **443**, 3631–3642
- McDaniel A., Jeltema T., Profumo S., 2021, *J. Cosmology Astropart. Phys.*, **2021**, 020
- Meshveliani T., Zavala J., Lovell M. R., 2023, *Phys. Rev. D*, **107**, 083010
- Metcalf R. B., Zhao H., 2002, *ApJ*, **567**, L5
- Metcalf R. B., et al., 2019, *A&A*, **625**, A119
- Minor Q. E., Kaplinghat M., Li N., 2017, *ApJ*, **845**, 118
- Minor Q., Kaplinghat M., Chan T. H., Simon E., 2021a, *MNRAS*, **507**, 1202
- Minor Q., Gad-Nasr S., Kaplinghat M., Vegetti S., 2021b, *MNRAS*, **507**, 1662
- Nadler E. O., Birrer S., Gilman D., Wechsler R. H., Du X., Benson A., Nierenberg A. M., Treu T., 2021, *ApJ*, **917**, 7
- Navarro J. F., Frenk C. S., White S. D. M., 1996, *ApJ*, **462**, 563
- Nishikawa H., Boddy K. K., Kaplinghat M., 2020, *Phys. Rev. D*, **101**, 063009
- Oldham L., et al., 2017, *MNRAS*, **465**, 3185
- Ostdiek B., Diaz Rivero A., Dvorkin C., 2022a, *ApJ*, **657**, L14
- Ostdiek B., Diaz Rivero A., Dvorkin C., 2022b, *ApJ*, **927**, 83
- Padfield D., 2010, in 2010 IEEE Computer Society Conference on Computer Vision and Pattern Recognition. pp 2918–2925, doi:[10.1109/CVPR.2010.5540032](https://doi.org/10.1109/CVPR.2010.5540032)
- Padfield D., 2012, *IEEE Transactions on Image Processing*, **21**, 2706
- Pen U.-L., Mao S., 2006, *MNRAS*, **367**, 1543
- Perreault-Levasseur L., Hezaveh Y. D., Wechsler R. H., 2017, *ApJ*, **850**, L7
- Peter A. H. G., Rocha M., Bullock J. S., Kaplinghat M., 2013, *MNRAS*, **430**, 105
- Planck Collaboration et al., 2020, *A&A*, **641**, A6
- Pullen A. R., Benson A. J., Moustakas L. A., 2014, *ApJ*, **792**, 24
- Rexroth M., Natarajan P., Kneib J.-P., 2016, *MNRAS*, **460**, 2505
- Rezaei S., McKean J. P., Biehl M., de Roo W., Lafontaine A., 2022, *MNRAS*, **517**, 1156
- Robertson M., Lewis A., 2023, *J. Cosmology Astropart. Phys.*, **2023**, 048
- Robertson A., Harvey D., Massey R., Eke V., McCarthy I. G., Jauzac M., Li B., Schaye J., 2019, *MNRAS*, **488**, 3646
- Rocha M., Peter A. H. G., Bullock J. S., Kaplinghat M., Garrison-Kimmel S., Oñorbe J., Moustakas L. A., 2013, *MNRAS*, **430**, 81
- Rojas K., et al., 2023, *MNRAS*, **523**, 4413
- Sagunski L., Gad-Nasr S., Colquhoun B., Robertson A., Tulin S., 2021, *J. Cosmology Astropart. Phys.*, **2021**, 024
- Sameie O., Yu H.-B., Sales L. V., Vogelsberger M., Zavala J., 2020, *Phys. Rev. Lett.*, **124**, 141102
- Schaefer C., Geiger M., Kuntzer T., Kneib J. P., 2018, *A&A*, **611**, A2
- Schneider P., 2019, *A&A*, **624**, A54
- Schneider P., Seitz C., 1995, *A&A*, **294**, 411
- Schneider P., Sluse D., 2013, *A&A*, **559**, A37
- Schneider P., Sluse D., 2014, *A&A*, **564**, A103
- Schneider A., Smith R. E., Macciò A. V., Moore B., 2012, *MNRAS*, **424**, 684
- Schneider A., Smith R. E., Reed D., 2013, *MNRAS*, **433**, 1573
- Serjeant S., 2014, *ApJ*, **793**, L10
- Serjeant S., 2017, *Publication of Korean Astronomical Society*, **32**, 251
- Shao S., Gao L., Theuns T., Frenk C. S., 2013, *MNRAS*, **430**, 2346
- Sheth R. K., Tormen G., 1999, *MNRAS*, **308**, 119
- Sheth R. K., Mo H. J., Tormen G., 2001, *MNRAS*, **323**, 1–12
- Shu Y., et al., 2016, *ApJ*, **833**, 264
- Spergel D. N., Steinhardt P. J., 2000, *Phys. Rev. Lett.*, **84**, 3760
- Springel V., et al., 2008, *MNRAS*, **391**, 1685
- Tulin S., Yu H.-B., Zurek K. M., 2013a, *Phys. Rev. D*, **87**, 115007
- Tulin S., Yu H.-B., Zurek K. M., 2013b, *Phys. Rev. Lett.*, **110**, 111301
- Tunruh S., Schneider P., Sluse D., 2017, *A&A*, **601**, A77
- Vegetti S., Koopmans L. V. E., 2009a, *MNRAS*, **392**, 945
- Vegetti S., Koopmans L. V. E., 2009b, *MNRAS*, **400**, 1583
- Vegetti S., Vogelsberger M., 2014, *MNRAS*, **442**, 3598
- Vegetti S., Czoske O., Koopmans L. V. E., 2010a, *MNRAS*, **407**, 225
- Vegetti S., Koopmans L. V. E., Bolton A., Treu T., Gavazzi R., 2010b, *MNRAS*, **408**, 1969
- Vegetti S., Lagattuta D. J., McKean J. P., Auger M. W., Fassnacht C. D., Koopmans L. V. E., 2012, *Nature*, **481**, 341
- Vegetti S., et al., 2023, *arXiv e-prints*, p. [arXiv:2306.11781](https://arxiv.org/abs/2306.11781)
- Vernardos G., Tsagkatakis G., Pantazis Y., 2020, *MNRAS*, **499**, 5641
- Viel M., Becker G. D., Bolton J. S., Haehnelt M. G., 2013, *Phys. Rev. D*, **88**, 043502
- Villasenor B., Robertson B., Madau P., Schneider E., 2023, *Phys. Rev. D*, **108**, 023502
- Virtanen P., et al., 2020, *Nature Methods*, **17**, 261
- Vogelsberger M., Zavala J., Loeb A., 2012, *MNRAS*, **423**, 3740
- Wagner-Carena S., Aalbers J., Birrer S., Nadler E. O., Darragh-Ford E., Marshall P. J., Wechsler R. H., 2023, *ApJ*, **942**, 75
- Weiner C., Serjeant S., Sedgwick C., 2020, *Research Notes of the American Astronomical Society*, **4**, 190
- Wertz O., Orthen, Bastian Schneider, Peter 2018, *A&A*, **617**, A140
- Wilde J., Serjeant S., Bromley J. M., Dickinson H., Koopmans L. V. E., Metcalf R. B., 2022, *MNRAS*, **512**, 3464
- Xu D. D., Mao S., Cooper A., Gao L., Frenk C., Angulo R., Helly J., 2012, *MNRAS*, **421**, 2553
- Yang D., Yu H.-B., 2022, *J. Cosmology Astropart. Phys.*, **09**, 077
- Yang S., Du X., Benson A. J., Pullen A. R., Peter A. H. G., 2020, *MNRAS*, **498**, 3902
- Yang D., Nadler E. O., Yu H.-B., Zhong Y.-M., 2023a, *arXiv e-prints*, p. [arXiv:2305.16176](https://arxiv.org/abs/2305.16176)
- Yang S., Du X., Zeng Z. C., Benson A., Jiang F., Nadler E. O., Peter A. H. G., 2023b, *ApJ*, **946**, 47
- Zeng Z. C., Peter A. H. G., Du X., Benson A., Kim S., Jiang F., Cyr-Racine F.-Y., Vogelsberger M., 2022, *MNRAS*, **513**, 4845
- Zhang G., Mishra-Sharma S., Dvorkin C., 2022, *MNRAS*, **517**, 4317
- Zhong Y.-M., Yang D., Yu H.-B., 2023, *MNRAS*, **526**, 758
- Çağan Şengül A., Tsang A., Diaz Rivero A., Dvorkin C., Zhu H.-M., Seljak U., 2020, *Phys. Rev. D*, **102**, 063502
- Şengül A. c., Dvorkin C., 2022, *MNRAS*, **516**, 336
- Şengül A. c., Dvorkin C., Ostdiek B., Tsang A., 2022, *MNRAS*, **515**, 4391

APPENDIX A: DETERMINING THE CORE DENSITY

In this appendix, we present briefly the process for calculating the value of the core radius to scale radius ratio, as stated in [Gilman et al. \(2021\)](#).

Rewrite the equation (5).

$$\rho(x, \beta, \tau) = \frac{\rho_s}{(x^a + \beta^a)^{\frac{1}{a}} (1+x)^2} \frac{\tau^2}{\tau^2 + x^2} \quad (\text{A1})$$

If we set the core density ρ_0 to $\rho(0, \beta, \tau) = \rho_0$, we get

$$\beta = \frac{r_c}{r_s} = \frac{\rho_s}{\rho_0}, \quad (\text{A2})$$

which determines the core radius r_c . [Gilman et al. \(2021\)](#) used a simple Jeans modelling approach previously proposed by [Kaplinghat et al. \(2016\)](#) to compute the core density ρ_0 and velocity dispersion v_{rms} . Dark matter particles scatter more efficiently near the centre of the halo, where the density of dark matter particles is greatest. As a result, [Kaplinghat et al. \(2016\)](#) divide the halo into two regions delineated by a distinctive radius r_1 , where this radius r_1 meets the condition:

$$\rho_{\text{NFW}}(r_1) \langle \sigma v \rangle t_{\text{halo}} = 1, \quad (\text{A3})$$

where $\langle \sigma v \rangle$ describes the scattering rate given the cross-section σ

Table B1. The mean number of haloes and core-collapsed haloes in our SIDM realizations used to obtain the results shown in Figs. 7 and B1. Notations $\langle N_{\text{SH}} \rangle$, $\langle N_{\text{LOSH}} \rangle$, $\langle N_{\text{cc,SH}} \rangle$, and $\langle N_{\text{cc,LOSH}} \rangle$ represent the mean numbers of subhaloes, line-of-sight haloes, core-collapsed subhaloes, and core-collapsed line-of-sight haloes, respectively.

v_0 [kms $^{-1}$]	30		
σ_0 [cm 2 g $^{-1}$]	5	25	50
$\langle N_{\text{SH}} \rangle$	2032		
$\langle N_{\text{LOSH}} \rangle$	1575		
$\langle N_{\text{cc,SH}} \rangle$	4	408	833
$\langle N_{\text{cc,SH}} \rangle / \langle N_{\text{SH}} \rangle$	0.002	0.201	0.410
$\langle N_{\text{cc,LOSH}} \rangle$	0	2	62
$\langle N_{\text{cc,LOSH}} \rangle / \langle N_{\text{LOSH}} \rangle$	0.0	0.001	0.039

and the relative velocity v , and ρ_{NFW} is the density of the NFW (Navarro et al. 1996) profile. At radius, $r > r_1$, Kaplinghat et al. (2016) assume that the density profile acts like an NFW profile, which is similar to collisionless CDM particles due to low dark matter self-interactions. By assuming that haloes collapse at redshift $z = 10$, we calculate the halo age t_{halo} as a function of z . The density profile of the isothermal solution ρ_{iso} is determined using the radial Jeans equation,

$$v_{\text{rms}}^2 \nabla \rho_{\text{iso}} = -\rho_{\text{iso}} \nabla \Phi \quad (\text{A4})$$

assuming hydrostatic equilibrium due to dark matter self-interactions. The differential equation for ρ_{iso} can be expressed using Poisson's equation $\nabla^2 \Phi = 4\pi G \rho_{\text{iso}}$ followed by the total gravitational potential Φ from dark matter as

$$v_{\text{rms}}^2 \nabla^2 \ln \rho_{\text{iso}} = -4\pi G \rho_{\text{iso}}. \quad (\text{A5})$$

This differential equation of the model with two unknowns, v_{rms} and ρ_0 , is solved using the boundary conditions $\rho_{\text{iso}}(0) = \rho_0$ and $\rho'_{\text{iso}}(0) = 0$. Since baryons are subdominant inside dark matter haloes in the mass range we consider in our simulations, we ignore their contribution to the mass of the dark matter haloes while solving these differential equations. According to Gilman et al. (2021), PYHALO employs a grid-based search approach to identify the best-fitting values for ρ_0 and v_{rms} until it meets the following two conditions at r_1 to 1% precision. The first condition states that the amplitude of the density of the isothermal solution ρ_{iso} at r_1 matches that of the NFW profile ρ_{NFW} at r_1 , and the second condition states that the enclosed mass of the isothermal solution within r_1 must equal that of the NFW profile with no interactions.

APPENDIX B: RELATIVE DIFFERENCES BETWEEN SIDM AND CDM MULTIPOLES

In this appendix, the relative differences between the CDM and the SIDM two-point correlation multipoles discussed in Section 4.1 are shown in Figs. B1 and B2. Also, Table B displays the mean number of subhaloes, line-of-sight haloes, and core-collapsed haloes, as well as their fractions, as a function of the SIDM cross-section, to offer quantitative information regarding core collapse.

This paper has been typeset from a TeX/LaTeX file prepared by the author.

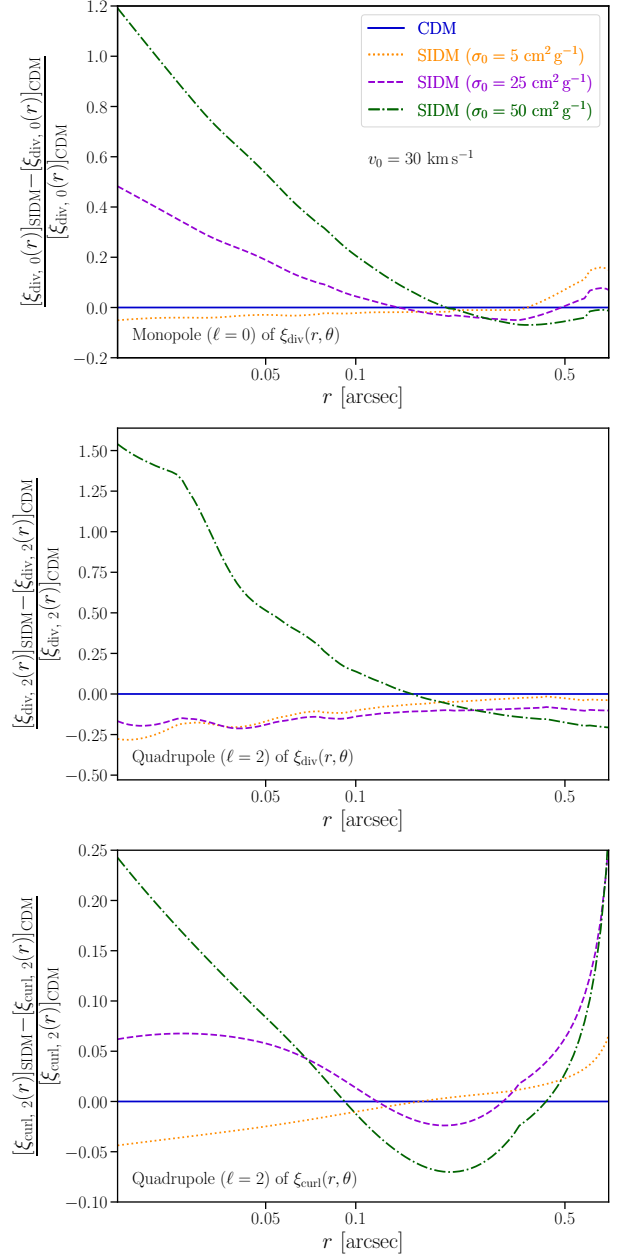


Figure B1. The relative difference between the two-point function multipoles (monopole (top panel) and the quadrupole (middle panel) of ξ_{div} , and the quadrupole moment (bottom panel) of ξ_{curl}) of the three SIDM models shown in Fig. 7 and the CDM model as a function of the velocity-dependent interaction cross-section normalization (σ_0). All three panels in this narrative have the same legend.

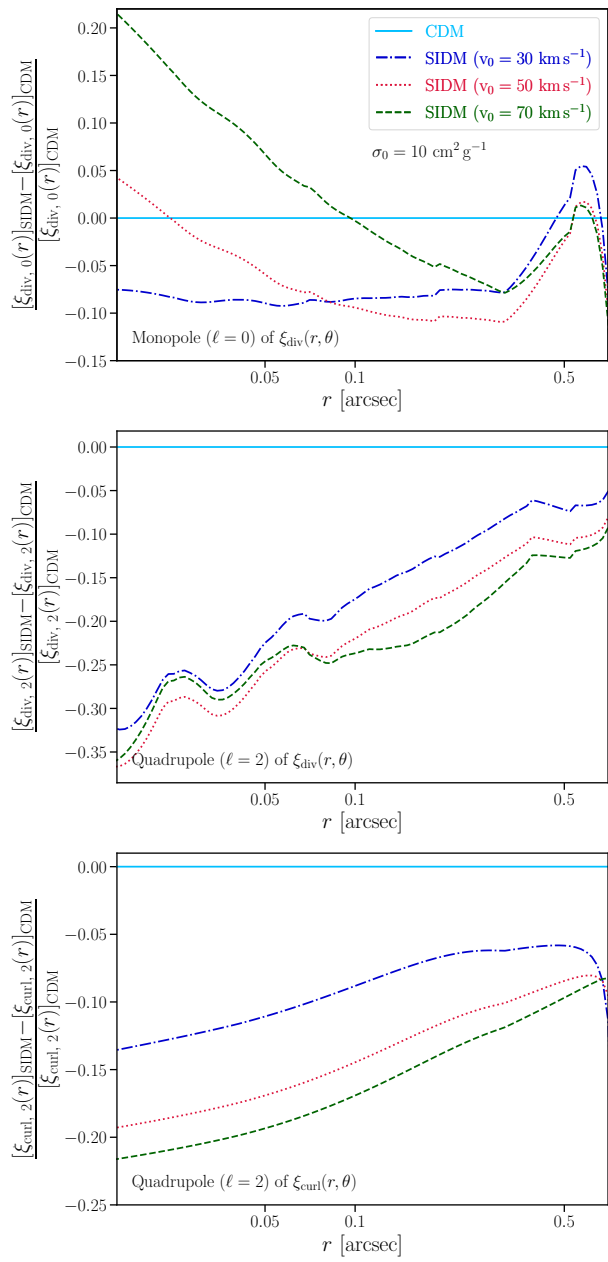


Figure B2. The same as in Fig. B1, but now as a function of the characteristic velocity (v_0) for the SIDM models depicted in Fig. 8.